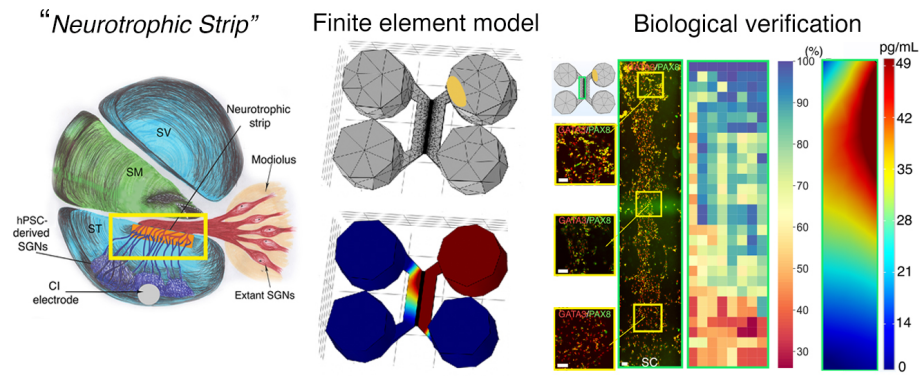


Graphical Abstract

Developing the Bioactive Cochlear Implant: Bridging the electrode–neuron gap through neurite guidance

Kevin T. Nella, Benjamin M. Norton, Hsiang-Tsun Chang, Rachel A. Heuer,
Christian B. Roque, Akihiro J. Matsuoka



Developing the Bioactive Cochlear Implant: Bridging the electrode–neuron gap through neurite guidance

Kevin T. Nella^{a,b}, Benjamin M. Norton^a, Hsiang-Tsun Chang^a, Rachel A. Heuer^a, Christian B. Roque^a, Akihiro J. Matsuoka^{a,c,d,e,*}

^a*Department of Otolaryngology–Head and Neck Surgery, Feinberg School of Medicine, Northwestern University, Chicago IL, 60611, USA*

^b*Department of Mechanical Engineering, Robert R. McCormick School of Engineering and Applied Science, Northwestern University, Evanston, IL., USA*

^c*Simpson Querrey Institute, Chicago IL, 60611, USA*

^d*Roxelyn and Richard Pepper Department of Communication Sciences and Disorders, School of Communication, Northwestern University, Evanston, IL., 60210, USA*

^e*The Hugh Knowles Center for Clinical and Basic Science in Hearing and its Disorders, Evanston, IL. 60210, USA*

Abstract

Although cochlear implant (CI) technology has allowed partial restoration of hearing over the last few decades, persistent challenges remain - including the deciphering of rich acoustic signals into a digital pulse-train signal. Among these challenges, the “electrode–neuron gap” poses the most significant obstacle to advancing past the current plateau in CI performance. Resulting issues include limited performance in noisy environments and a poor ability to decode intonation and music. We propose the development of a “neurotrophic strip”—a biological interface that doubly preserves endogenous spiral ganglion neurons (SGNs) while precisely directing the growth of neurites arising from transplanted human pluripotent stem cell (hPSC)-derived otic neuronal progenitors (ONPS), toward endogenous SGNs. We hypothesized that the Polyhedrin Delivery System (PODS®-human brain-derived neurotrophic factor [BDNF]) could stably

*Corresponding author: Akihiro J. Matsuoka, Department of Otolaryngology–Head and Neck Surgery, Feinberg School of Medicine, Northwestern University, 676 North St. Clair Street Suite 1325, Chicago, IL 60611, USA. E-mail addresses: amatsuok@nm.org, akihiro.matsuoka@northwestern.edu.

Email addresses: kevin.nella@northwestern.edu (Kevin T. Nella), benjamin.norton@northwestern.edu (Benjamin M. Norton), hsiangtsun.chang@gmail.com (Hsiang-Tsun Chang), racheuer@gmail.com (Rachel A. Heuer), christian.b.roq@gmail.com (Christian B. Roque), amatsuok@nm.org (Akihiro J. Matsuoka)

provide an adequate BDNF gradient to hPSC-derived ONPs, thereby simultaneously facilitating otic neuronal differentiation and directional neurite outgrowth. To test this hypothesis, we first devised a finite element model to simulate the *in vitro* BDNF gradient generated by PODS®. For biological verification, we validated the concept of the neurotrophic strip by using a multi-chamber microfluidic device, which mimics the *in vivo* micro-environment more accurately than conventional laboratory plates in terms of volume and concentrations of endogenous/exogenous factors. We were able to generate the optimal BDNF concentration gradient to enable survival, neuronal differentiation toward hPSC-derived SGNs, and directed neurite extension of hPSC-derived SGNs. The technique will allow us to further advance our concept of the “neurotrophic strip” by controlling neurite direction of transplanted hPSC-derived ONPs. This proof-of-concept study provides a step toward the next generation of CI technology.

Keywords: human pluripotent stem cells, finite element model, microfluidic device, neurotrophic factor, cochlear implant, neuroelectric interface, stem cell niche, spiral ganglion neurons

2010 MSC: 74S05, 62P10, 92C20

¹ **1. Introduction**

² The cochlear implant (CI), which provides functional restoration in patients
³ with sensorineural hearing loss, forms a neuro-electronic interface with the pe-
⁴ ripheral auditory nervous system [1]. CI technology functions by electrically
⁵ stimulating the extant population of auditory neurons (i.e., spiral ganglion neu-
⁶ rons [SGNs]). Although CI technology has allowed partial restoration of hearing
⁷ for this patient population over the last few decades, persistent challenges, in-
⁸ cluding the deciphering of rich acoustic signals into digital pulse-train signals,
⁹ remain. Among these challenges, the “electrode-neuron gap” poses the most
¹⁰ significant obstacle to advancing past the current plateau in CI performance.
¹¹ This phenomenon results in limited performance in noisy environments and poor
¹² ability to decode intonation and music [2], arguably decreasing quality of life.
¹³ The gap exists between the CI electrode and the target membranes of dendrites
¹⁴ in surviving endogenous SGNs [3]. It results in the requirement of larger CI
¹⁵ excitation fields, leading to current spread that excites and therefore disables
¹⁶ the neighboring electrodes, resulting in fewer information channels to the brain,
¹⁷ all within discrete time steps [2, 4]. This can develop into a vicious cycle as
¹⁸ fewer information channels to the brain also prompt the need for larger CI ex-
¹⁹ citation fields. The length of the gap generally spans hundreds of μm [5, 6].
²⁰ Hahnewald et al. demonstrated *in vitro* that energy needed to elicit a response
²¹ can be reduced by up to 20% by reducing the distance from 40 to zero μm (by
²² growing early postnatal mouse SGN explants on a microelectrode array) [4].

²³ To resolve the electrode-neuron gap *in vivo*, previous work has introduced
²⁴ the concept of a bioactive CI (Figure. 1A) [7, 8, 9]. The bioactive CI combines
²⁵ the current state-of-the-art CI technology with emerging stem cell-replacement
²⁶ therapy in the inner ear. In this scheme, transplanted human pluripotent stem
²⁷ cell (hPSC)-derived SGNs bridge the gap between the CI electrode and sur-
²⁸ viving endogenous SGNs. Neurotrophin gradients have been shown to guide
²⁹ hPSC grafts in spinal cord injury [10], direct growth of endogenous SGNs to-
³⁰ ward CI electrodes in the scala tympani [11], and enable transplanted hPSC

31 derived otic neuronal progenitors (ONPs) to grow neurites toward the modiolus
32 [9]. Although promising, these studies failed to observe adequate directional
33 neurite outgrowth toward endogenous SGNs (i.e., lack of synaptic connections
34 between hPSC grafts and endogenous SGNs), presumably preventing significant
35 improvements in functional recovery of hearing.

36 To confront this issue, we propose the development of a “neurotrophic strip”—a
37 biological interface that doubly preserves endogenous SGNs while precisely di-
38 recting the growth of neurites arising from transplanted hPSC-derived ONPs
39 toward the endogenous SGNs. The highlighted yellow-square area in Figure
40 1A shows a schematic diagram of this concept. Here, the neurotrophic strip
41 (shown as an orange rectangle in Figure 1A) stimulates neurite outgrowth from
42 both the hPSC-derived ONPs and the endogenous SGNs via a neurotrophic fac-
43 tor gradient [12]. While the concept of a neurotrophin gradient for directional
44 axonal growth has existed for a few decades, incorporating neurotrophin gradi-
45 ents into any tissue-engineered scaffold has been extremely challenging due to
46 the lack of self-sustaining neurotrophin delivery methods—their eventual deple-
47 tion triggers an accelerated decline in neurite growth and the survival of extant
48 SGNs [13, 14, 15]. One major contributor is the structurally unstable nature of
49 neurotrophins, which suffer from fragility and thermo-instability under normal
50 physiological conditions both *in vitro* and *in vivo*, leading to short half-lives typi-
51 cally ranging from minutes to hours [16]. This issue can be overcome by utilizing
52 the polyhedrin delivery system (PODS®)—a crystalline growth factor formu-
53 lation developed to enable long-term release of growth factors while dampening
54 degradation rates at the source [17, 18, 19] (Figure 1B). The PODS® technology
55 has adapted viral machinery to encase a chosen growth factor into polyhedrin
56 protein cases. The resultant growth factor co-crystals have slow degradation pro-
57 files under physiological conditions and, therefore, allow the sustained release of
58 embedded bioactive growth factor protein such as neurotrophins.

59 We reasoned that an bio-engineered scaffolding incorporated with PODS®
60 technology can establish a neuronal network between transplanted hPSC-derived
61 ONP grafts and extant SGNs in the inner ear. More specifically, we hypothesized

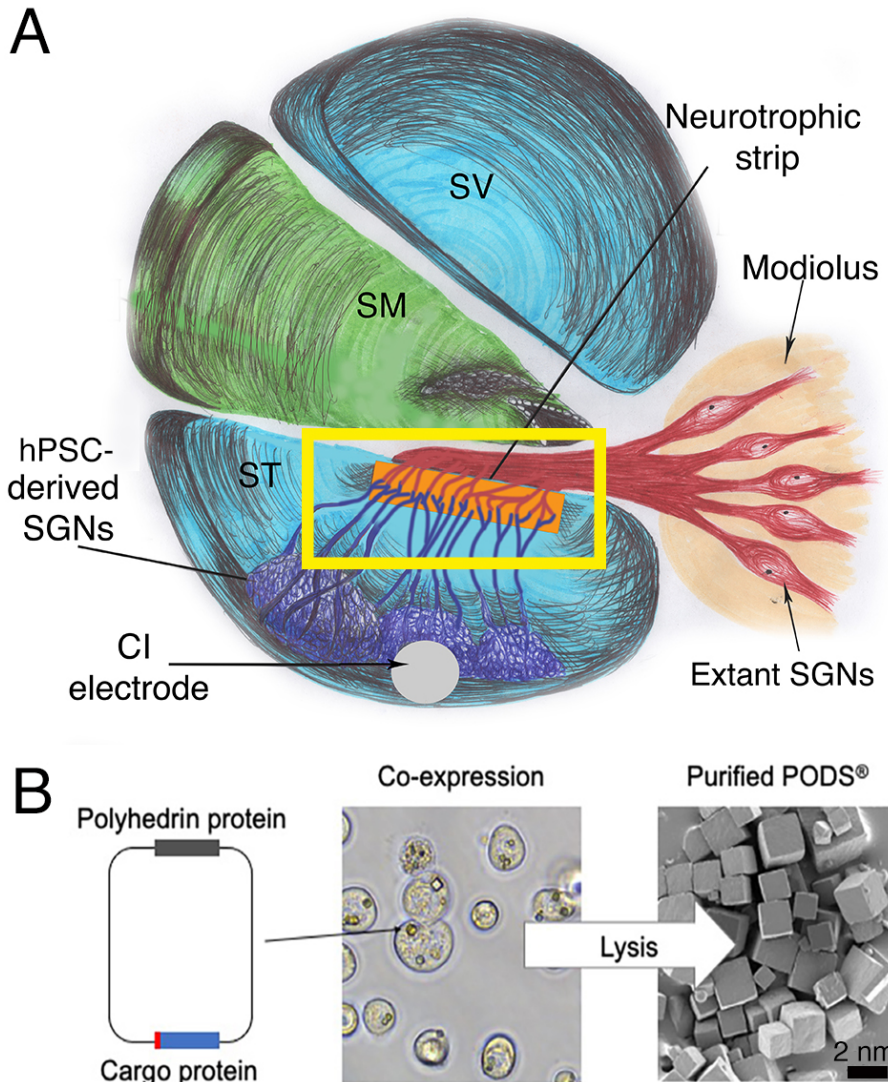


Figure 1: (A): A next-generation bioactive CI and a neurotrophic strip. The neural network in this scheme consists of a CI electrode, transplanted stem cell-derived SGNs, the neurotrophic strip, and extant/endogenous SGNs (red). Note that neuronal connection is largely absent with hair cells (not shown). (B): Polyhedrin Delivery System (PODS)®. PODS® crystals are cubic protein co-crystals produced by Sf9 cells (a clonal isolate of *Spodoptera frugiperda* Sf21 cells [IPLB-Sf21-AE], in which the polyhedrin protein and a second protein are co-expressed). This second protein is termed as the active, or cargo protein (Figure 1B, left). Inside the Sf9 cells, polyhedrin proteins self-assemble into cubic crystals (Figure 1B, center) while the active protein, tagged with a short peptide sequence, binds to the growing polyhedrin crystal. The crystals are extracted and purified by simple cell lysis and washes to remove cell debris (Scanning electron micrograph, Figure 1B, right).

that PODS[®]-human neurotrophin system could stably provide and maintain an adequate neurotrophin gradient to hPSC-derived ONPs, facilitating otic neuronal differentiation and directional neurite outgrowth. To test this hypothesis, we first devised a finite element model (FEM) to simulate the *in vitro* neurotrophin gradient generated by PODS[®]. In this study, we focus on the role of BDNF—the most studied of the neurotrophins in the inner ear, and the most vital for the functional recovery of damaged SGNs [20]. For biological validation and demonstration we used a multi-chamber microfluidic device, which mimics the *in vivo* micro-environment of the inner ear more so than conventional laboratory plates in terms of volume and concentrations of endogenous/exogenous factors [21].

2. Materials and Methods

2.1. Polyhedrin delivery system

The Polyhedrin Delivery System (PODS[®]-human BDNF [rhBDNF]) (Cell Guidance Systems, Cambridge, United Kingdom) was used as a self sustaining source of rhBDNF. PODS[®]-rhBDNF utilizes the polyhedrin protein formed by *Bombyx mori*, an insect from the moth family *Bombycidae*. A cargo protein (i.e., rhBDNF) is co-expressed within the polyhedrin crystal and is slowly released with degradation of the PODS[®] crystals by cell-secreted proteases (Figure 1B)[9, 18, 22].

2.2. Human pluripotent stem cell culture using dual-compartment microfluidic device

Human embryonic stem cells (hESCs: H7 and H9, passages number 25–35) and were obtained from WiCell Research Institute (Madison, Wisconsin, USA). Human induced pluripotent stem cells (hiPSCs: TC-1133HKK, passage number 22–35) were generated from human CD34+ cord blood cells using the four Yamanaka factors at Lonza (Walkersville, Maryland [MD], USA). The hiPSC cell line (TC-1133HKK) was kindly provided by Healios K.K. (Tokyo, Japan).

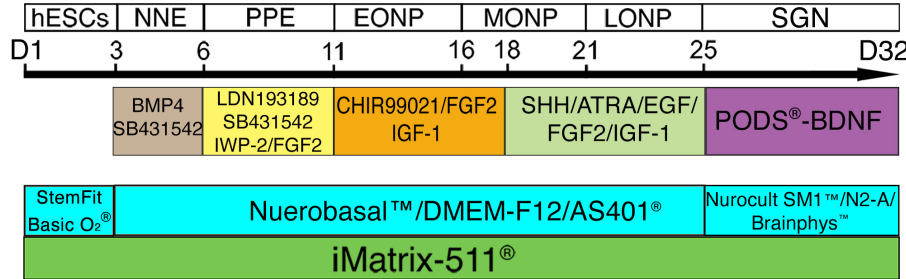


Figure 2: Overview of otic neuronal differentiation protocol for hPSCs. Please see detail in [8, 9, 23, 24] and the Supplemental Data. Each developmental stage is shown at the top, with key treatments shown below. NNE: nonneuronal ectoderm; PPE: preplacodal ectoderm; EONP: early-stage otic neuronal progenitor; MONP: mid-stage otic neuronal progenitor; LONP: late-stage otic neuronal progenitor; BMP4: bone morphogenetic protein 4; SHH: Sonic hedgehog; ATRA: all-trans retinoic acid; EGF: epidermal growth factor; IGF-1: insulin-like growth factor-1; FGF2: fibroblast growth factor 2; N2B27-CDM: chemically defined medium containing N2 and B27 supplements.

90 hPSC-derived ONPs were derived based on our previously established protocol
 91 (Supplemental Data) [8, 9, 23, 24]. A step-wise series of ligands and growth
 92 factors was added to a neuronal induction medium to promote hPSC differen-
 93 tiation toward the late-stage ONP lineage—mitotic progenitor population that
 94 generates the SGNs. (Figure 2).

95 Microfluidic devices provide a platform for specifically evaluating axonal re-
 96 generation [25]. Here, multi-chamber microfluidic devices, Xona™ Microfluidics
 97 XC150 and XC450 (Xona™ Microfluidics, Research Triangle Park, North Car-
 98 olina, USA), were used for computational calculation and biological validation
 99 (Figure 3A–B). The Xona™ device allows for neurites to grow toward growth
 100 factors in the opposite chamber while limiting migration of derived ONP cell
 101 bodies due to specific dimensions of the device. Additionally, the microchannel
 102 array between the two chambers mimics the porous bony separation between
 103 the modiolus (where extant SGNs are localized) and the scala tympani (where
 104 the biohybrid CI will be implanted). Thus the diffusion profile of the released
 105 rhBDNF *in vitro* more accurately predicts that of the *in vivo*.

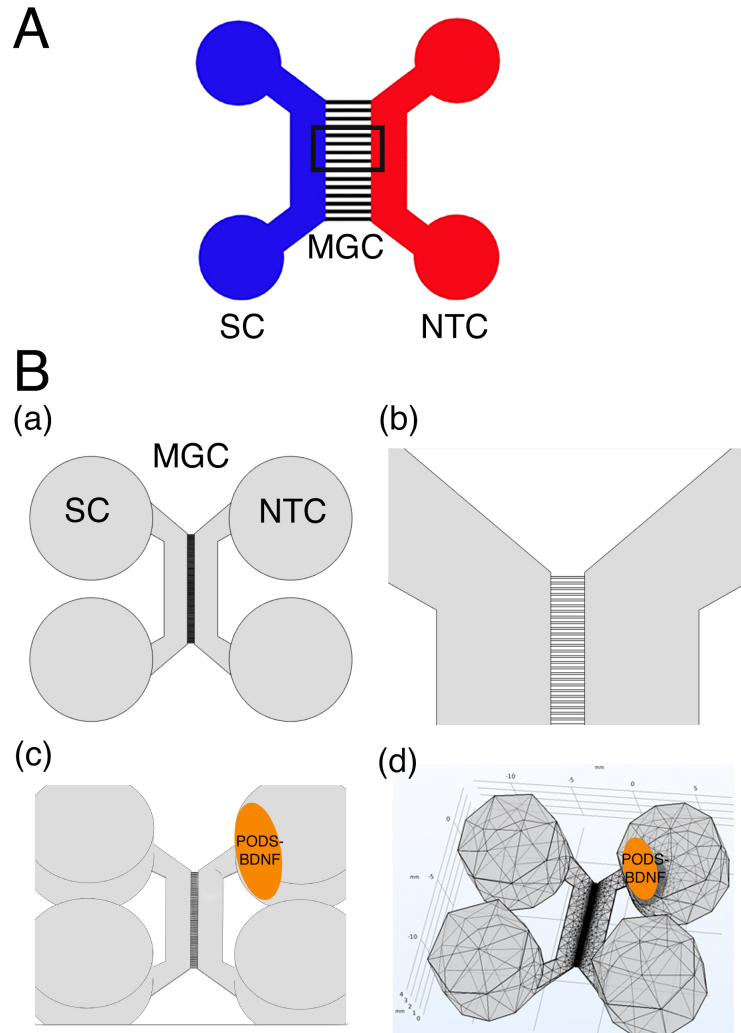


Figure 3: (A): Schematic specification of a Xona™ Microfluidics XC 450. Two main channels (somal compartment (SC) and neurotrophin compartment (NTC)) on either side are connected by a micro-groove channel (MGC) spanning $450 \mu\text{m}$ with a width of $10 \mu\text{m}$ (black square). The somal compartment contains hPSC-derived late-stage ONPs (shown in black), while the neurotrophin compartment contains the secreted factors (i.e., BDNF) that are released from PODS®-rhBDNF crystals. (B):(a) Xona™ Microfluidics XC450 device geometry, created at a 1:1 scale with Autodesk Inventor®, in which the diffusion profile of the released BDNF was modeled and tested. (b) Detail of the microchannels joining the two compartments of the Xona™ Microfluidics XC450. (c) Xona™ Microfluidics XC450 device showing the optimized area and geometry to localize PODS® containing rhBDNF (yellow ellipsoid area). (d): Mesh geometry of the Xona™ XC450 generated with Autodesk Inventor, depicting the localized volume of PODS®-rhBDNF ($1 \mu\text{L}$) as an ellipsoid disk.

106 The devices were washed and coated with poly-L-ornithine (PLO, 20 μ g/mL
107 in H₂O, Sigma-Aldrich, St. Louis, Missouri [MO], USA) and recombinant
108 laminin-511 (iMatrix-511, 0.5 mg/mL, Nacalai USA, San Diego, California [CA],
109 USA) according to the manufacturer-outlined protocol. Next, approximately
110 1.75 x 10⁵ cells (in 20 μ L of media) were added through the top and bottom left
111 wells to the somal compartment (i.e., the total amount of 3.5 x 10⁵ hPSC-derived
112 ONPs were added).

113 PODS®-rhBDNF were placed in the top right well of the neurotrophin com-
114 partment (Figure 3A–B) to generate a BDNF concentration gradient to promote
115 directional neurite growth. hPSC-derived ONPs were cultured for 7 days in the
116 Xona™ device to induce otic neuronal differentiation. Note that due to our
117 use of the microfluidic device, high-density cell cultures were induced to facil-
118 itate molecular studies as well as the generation of a more biologically relevant
119 neuronal phenotype (i.e., otic lineage) [25]. Media was topped off daily after
120 imaging (from 20–40 μ L per well).

121 *2.3. Three-dimensional finite element model*

122 We used finite element analysis (FEA) to simulate the BDNF concentration
123 gradient in a multi-chamber microfluidic device during release and subsequent
124 degradation. FEA is a computational numerical technique, which approximates
125 mathematical solutions to partial differential equations (PDEs) that appropri-
126 ately simulate complex real-world problems. In this study, the finite element
127 model allowed us to predict the concentration gradient with respect to time in
128 the multi-chamber microfluidic device, depending on the number of PODS®-
129 rhBDNF introduced into the system. To solve the finite element model, we used
130 COMSOL® Multiphysics (version 5.6 [released on November 11, 2020], COM-
131 SOL, Inc., Burlington, Massachusetts [MA], USA), which is a finite element
132 method solution tool for engineering and scientific research computations. We
133 used sustained-release kinetics for PODS®-rhBDNF determined from an ELISA
134 study (see next subsection) as well as data from a previous study from our group
135 [9]. Device geometry was generated at a 1:1 scale using Autodesk® Inventor

136 2019.0.2 (Autodesk, Mill Valley, CA, USA) (Figure 3B). The computational
137 analysis was implemented on a high-performance desktop computer platform
138 equipped with a CPU (AMD Ryzen Threadripper 3990X 64-Core, 128-Thread
139 @ 4.3 GHz) with 64 GB RAM, and two GPU cards (NVIDIA GeForce RTX
140 3080Ti,12GB 384-bit GFF6X Graphics card).

141 *2.4. Enzyme-linked immunosorbent assay for brain-derived neurotrophic factor*

142 In order to determine the release and degradation kinetics of PODS[®]-
143 rhBDNF, an experiment measuring concentrations at sequential time points was
144 performed. To measure the concentration of rhBDNF secreted from PODS[®]-
145 rhBDNF crystals, the culture media from both a control and an experimental
146 condition were collected at each time point and immediately stored at -80°C
147 before running an enzyme-linked immunosorbent assay (ELISA) after the final
148 collection. The same method was applied to measure the degradation kinetics
149 of rhBDNF protein with a carrier protein (Bovine Serum Albumin [BSA])
150 (#248-BDB-050, R&D Systems, Minneapolis, Minnesota, USA). Experimen-
151 tal conditions were culture media enriched with 10% fetal bovine serum (FBS)
152 (Thermo Fisher Scientific, Waltham, MA, USA). All samples were quantified
153 with a BDNF ELISA kit (# BGK23560; PeproTech, Rocky Hill, New Jersey,
154 USA), and the results were analyzed with a Synergy HTX Multi-Mode Reader
155 (BioTek, Winooski, Vermont, USA) at a 450 nm wavelength, as instructed by
156 the manufacturer. Release and degradation kinetics were then calculated using
157 MATLAB Curve Fitting Toolbox (MathWorks, Natick, CA, USA).

158 *2.5. Sodium dodecyl sulphate-polyacrylamide gel electrophoresis*

159 Sodium dodecyl-sulfate polyacrylamide gel electrophoresis (SDS-PAGE) is
160 commonly used as a method to separate proteins with molecular masses be-
161 tween 5 and 250 kDa [26], a range of which is suitable for detecting human
162 BDNF protein (molecular weight [MW]: 14kDa [27]) and polyhedrin (MW: ~29
163 kDa [22]). In this study, SDS-PAGE was used to assess the molar ratio of
164 BDNF to polyhedrin in each sample. Briefly, each protein sample was diluted

165 in deionized water and mixed with 6x Laemmli sample buffer (Bio-Rad Labora-
166 tories, Inc., Des Plaines, Illinois [IL], USA) containing 2-mercaptoethanol and
167 heated at 100°C for 5 to 20 minutes. Samples were then loaded into precast
168 Mini-PROTEAN TGX 4-15% polyacrylamide mini-gels (Bio-Rad Laboratories,
169 Inc., Des Plaines, IL, USA). Then, 5 mL of Precision Plus Protein Kaleido-
170 scope Prestained Protein Standards (Bio-Rad Laboratories, Inc., Des Plaines,
171 IL, USA) were loaded in each gel run. Electrophoresis was performed at room
172 temperature for approximately 90 minutes using a constant voltage (100V) in
173 1x solution of Tris-Glycine-SDS electrophoresis buffer (Bio-Rad Laboratories,
174 Inc., Des Plaines, IL, USA) until the dye front reached the end of the 60 mm
175 gel. After electrophoresis, the mini-gels were rinsed with deionized water 3
176 times for 5 minutes and were subsequently incubated in SimplyBlue™ SafeStain
177 (ThermoFisher Scientific, Waltham, MA, USA) for one hour at room temper-
178 ature with gently agitation. Images obtained from gels were analyzed using
179 ImageJ 1.53g (December 4, 2020, the National Institutes of Health, Bethesda,
180 MD, USA [28]). The calculated molar ratio was applied to the COMSOL®
181 Multiphysics model to accurately predict the amount of rhBDNF released from
182 PODS®-rhBDNF. SDS-PAGE was performed according to the manufacturer's
183 technical guide (Bio-Rad Laboratories, Inc., Des Plaines, IL, USA).

184 *2.6. Western Blot*

185 The identity of the BDNF protein detected by SDS PAGE was verified by
186 western blot (Bio-Rad Laboratories, Inc., Des Plaines, IL, USA). Briefly, the
187 polyvinylidene difluoride (PVDF) membrane was prepared in methanol for 30
188 seconds before soaking in 1x Tris-Glycine-Methanol transfer buffer for 10 min-
189utes. Wet transfer was performed at 4°C for approximately 60 minutes using a
190 constant voltage (100V) in 1X solution of Tris-Glycine-Methanol transfer buffer.
191 After transfer, the membrane was briefly rinsed with 1X Tris-buffered saline
192 Tween-20 (TBST) and was subsequently blocked in 5% BSA in TBST for 24
193 hours at 4°C with gentle agitation. The membrane was then rinsed with 1x
194 TBST before incubating in BDNF polyclonal antibody (ThermoFisher Scien-

tific, Waltham, MA, USA) diluted to 1:1500 in 1% BSA in TBST for 24 hours at 4°C with gentle agitation. Following incubation, the membrane was rinsed in 1x TBST 5 times for 5 minutes to remove unbound primary antibody. Then, the membrane was incubated in Goat anti-Rabbit IgG (H+L) horseradish peroxidase (HRP) conjugated secondary antibody (ThermoFisher Scientific, Waltham, MA, USA) diluted to 1:5000 in 1% BSA in TBST for one hour at room temperature with gentle agitation. Following incubation, the membrane was rinsed in 1x TBST 5 times for 5 minutes to remove unbound secondary antibody. For sensitive detection, the membrane was treated with Pierce™ ECL Western Blotting Substrate (ThermoFisher Scientific, Waltham, MA, USA), and visualized using an Azure 600 Digital Imager (Azure Biosystems, Dublin, CA, USA). Electrophoresis buffer for sample condition and run condition was summarized in Supplementary Table S1.

2.7. Immunocytochemistry and image acquisition

Glass coverslips (Corning Inc., Corning, New York, USA) were coated with poly-d-lysine (PDL) (#A3890401, ThermoFisher Scientific, Waltham, MA, USA) and poly-ornithine (PLO) (# A-004-C, MilliporeSigma, St. Louis, MO, USA) affixed to a somal compartment as per the manufacturer's instructions. A total of 100,000 dissociated hPSC-derived ONPs were plated onto a somal compartment of the device. On Day 7, 4% (w/v) paraformaldehyde (PFA) (ThermoFisher Scientific, Waltham, MA, USA) was added to the compartments for 20 minutes to fix the cells. ICC was used to stain for GATA3, PAX8, and beta-III tubulin. These three proteins have shown to appropriately characterize ONPs in our previous studies [8, 9, 24]. Following PBS wash, cultures were blocked with 5% BSA at room temperature for 1 hour. Cultures were then incubated overnight at 4°C on a shaker plate in primary antibody solution using Rabbit anti-Beta-III-Tubulin (1:100, Abcam, Cambridge, MA, USA), Goat anti-PAX8 (1:500, Abcam, Cambridge, MA, USA), and Mouse anti-GATA3 (1:500, R&D Systems, Minneapolis, MN, USA). Following PBS washes, cultures were incubated at room temperature for 90 minutes on a shaker plate in sec-

225 ondary antibody solution composed of Alexafluor647 anti-Rabbit (1:1000, Ther-
226 moFisher Scientific, St. Louis, MO, USA), Alexafluor488 anti-Goat (1:1000,
227 ThermoFisher Scientific, St. Louis, MO, USA), and Alexafluor594 anti-Mouse
228 (1:1000, ThermoFisher Scientific, St. Louis, MO, USA) in 1% BSA. Following
229 PBS -/- washes, cultures were incubated with DAPI for 20 minutes (300 nM,
230 ThermoFisher Scientific, St. Louis, MO, USA). Secondary antibody controls
231 were performed each time multiple primary antibodies were used [29]. Label-
232 ing controls (detection controls) were performed for a sample from each batch
233 of hPSC culture [29]. See Supplementary Figure S1 for exemplary figures for
234 these control conditions. Results were imaged using a Nikon Ti2 Widefield
235 Laser Microscope System (Nikon, Tokyo, Japan). Phase-contrast images were
236 captured on a Nikon Eclipse TE2000-U inverted microscope (Nikon, Tokyo,
237 Japan). All fluorescence images were acquired on a Zeiss LSM 510 META laser-
238 scanning confocal microscope (Carl Zeiss, Oberkochen, Germany), a Nikon Ti2
239 laser laser-scanning confocal microscope (Nikon, Tokyo, Japan), or a Leica SP5
240 laser-scanning confocal microscope (Leica, Welzlar, Germany). Observers were
241 blinded to the conditions during imaging and tracing. In general, the images
242 were processed with a Image J ver. 1.53j or Matlab R2020b. Further detail on
243 image acquisition and quantification of fluorescent-positive cells can be found
244 in the Supplemental Data.

245 *2.8. Preferred cell orientation analysis*

246 Collective cell migration, where cells organized in a tightly connected fashion
247 migrate as cohesive structures, is a critical biological process to highlight the
248 neurotrophin diffusion gradient profile [30]. To evaluate this process, time-lapse
249 acquisition of images of the Xona™ device was performed using an inverted mi-
250 croscope (Nikon Eclipse TS100, Tokyo, Japan) at Day 1, 3, 5, and 7. Due to the
251 high cell density required for hPSC-ONPs to survive in the somal compartment
252 of the Xona™ device, images were not amenable to manual analysis in most of
253 the cases. To circumvent this problem, we performed a series of image pre-
254 processings that are mainly based on modified binarization-based extraction of

255 alignment score methods with some modifications [31]. We used MATLAB Im-
256 age Processing Toolbox R2020b (version 9.9.0.1495850, September 30th, 2020,
257 Mathworks, Natick, MA) for analysis. Please see Supplementary Figure S2 for
258 further detail. The analysis of directional data in general represents a particu-
259 lar challenge: there is no reason to designate any particular point on the circle
260 as zero, as it is somewhat arbitrary depending on where one sets a coordinate
261 [32, 33]. In this study, we used polar coordinates to determine the directionality
262 of preferred cell orientation. For this analysis, we again used MATLAB Image
263 Processing Toolbox R2020b. See detailed discussion on how we determined the
264 preferred cell orientation in Supplementary Figure S3.

265 *2.9. Neurite alignment vector assay, neurite growth assay and cell migration*
266 *assay*

267 The microfluidic device allowed us to culture hPSC-derived ONPs in a po-
268 larized manner and to directly isolate/analyze neurites. To evaluate the neurite
269 projection into the neurotrophin compartment by derived otic neurons cultured
270 in the somal compartment, we performed a neurite alignment vector assay. We
271 also evaluated the length of neurites that grew from hPSC-derived ONPs. For
272 these purposes, hPSC-derived ONPs were cultured in a Xona™ XC450 for seven
273 days and then immunostained with *beta*-III tubulin and DAPI. We used two
274 ImageJ plug-in toolkits, NeuriteTracer and NeuronJ, to assess neurite align-
275 ment and neurite growth [34, 35]. Due to the bipolar nature of hPSC-derived
276 ONPs/SGNs, we measured the two longest neurites from the cells [24, 36].
277 Please see Supplementary Figure S4 for detailed description of this analysis. We
278 used hPSC-derived ONPs cultured with 800,000 PODS®-rhBDNF as a positive
279 control. The number 800,000 was chosen based on our FEM in that there was
280 no neurotrophin gradient in a somal compartment. As a negative control, we
281 used 20 ng/mL of recombinant human BDNF. To evaluate cell migration across
282 a microgroove channel, we performed cell migration analysis. We manually
283 counted the number of ONPs that migrated from the somal compartment into
284 the microchannels, as well as the neurotrophin compartment.

285 *2.10. Statistical analysis*

286 When appropriate, and as indicated in each figure, statistical analysis was
287 performed. Experimental values are typically expressed as mean and standard
288 error (SE). The majority of the statistical analyses were performed with Python
289 3.9.6. (Python Software Foundation, Wilmington, Delaware, USA). The follow-
290 ing libraries were used for the statistical analysis: Scipy, Numpy, Matplotlib,
291 and Seaborn [37, 38, 39]. Normal distributions were assumed unless mentioned
292 otherwise. *P* values smaller than 0.05 were considered statistically significant.
293 For circular statistics, we derived the sample mean vector and its polar coor-
294 dinate. Mean and confidence intervals were calculated. We chose confidence
295 coefficient, *Q*, e.g. *Q* = 0.95. To analyze the axial nature of data, especially to
296 compute the mean vector angle, we doubled each angle and reduced the mul-
297 tiples modulo 360°. Please see detailed discussion in Supplementary Figure S3
298 and S5. The Rayleigh test of uniformity and V-test were performed to deter-
299 mine whether the samples differ significantly from randomness (i.e., where there
300 is statistical evidence of directionality). One-sample test for the mean angle was
301 performed to test whether the population mean angle is statistically different
302 from the given angle. In all of our circular statistics, von Mises distribution was
303 assumed and also verified. Circular statistics were performed using CircStat: A
304 MATLAB Toolbox [33, 40]. Please see detailed description of circular statistics
305 in Supplementary Figure S3 and S5. Experiments were done in three biological
306 replicates unless otherwise specified in Figure captions.

307 **3. Results**

308 The appropriate number of PODS®-rhBDNF crystals to induce an effective
309 neurotrophin gradient for otic neuronal differentiation and neurite outgrowth
310 was calculated using a three-dimensional FEA that predicts the concentration
311 profile of BDNF formed through the gradual release and diffusion of BDNF
312 from PODS®-rhBDNF. We first empirically tested two available microchannel
313 lengths—(i.e., Xona™-XC150 [150 μm] and Xona™-XC450 [450 μm]). This was

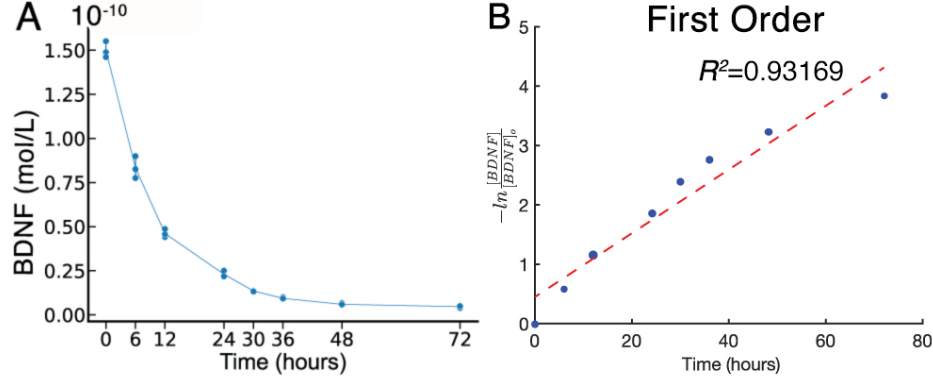


Figure 4: Chemical kinetics of Brain Derived Neurotrophic Factor (BDNF). (A): Concentration of rhBDNF in solution over 72 hours after initial application. (B): $\frac{1}{[BDNF]}$ data fit to first order curve. Please see other curve fit data in Supplemental Figure 1. Red line: fitted line, blue dots: individual data point. k_2 is defined as slope of fitted curve.

314 done initially because mass (i.e., BDNF) transport from the neurotrophin com-
 315 partment through the micro-groove channels into the somal compartment is an
 316 important factor in generating the concentration gradient *via* diffusion mixing.
 317 We determined that the Xona™ Microfluidics XC450 was more appropriate for
 318 this study as the XC-150's micro-groove channels were not long enough to gener-
 319 ate the appropriate concentration gradient throughout the somal compartment.
 320 This feature is relevant to human inner ear because the micro-groove channels in
 321 the Xona device simulates the presence of the osseous spiral lamina and modi-
 322 olus between the scala tympani and SGNs [41, 42]. Following device selection,
 323 we generated a three-dimensional geometry mesh of the Xona™ Microfluidics
 324 XC450 for the FEA (Figure 3B(d)). Please also see Supplementary Figure S6
 325 for detailed measurements of the mesh.

We then quantified the chemical kinetics of the degradation of PODS®-rhBDNF followed by the release and eventual degradation of the rhBDNF by ELISA testing (Figure 4) to establish the parameters for the FEA. Here, two consecutive chemical reactions occur: 1) the release of rhBDNF through degra-
 dation of PODS® crystals, and 2) the degradation of rhBDNF toward the degra-

dation product (Equation (1)).



326 where DP is the degradation product of the released rhBDNF, and k_1 and k_2
 327 are the rate constants ($\frac{1}{hour}$) for their respective reactions.

328 Degradation kinetics for rhBDNF was collected while monitoring rhBDNF
 329 concentration after introducing a predefined amount into a single well of solu-
 330 tion. The data obtained throughout the first 72 hours indicate an exponential
 331 decay, suggesting first order kinetics (Figure 4). To confirm this notion, we
 332 performed a linear and nonlinear least square analysis of the kinetic data with
 333 the MATLAB Curve Fitting Toolbox. We found that the corresponding R^2 was
 334 0.93169 for the first order curve-fit, confirming that the degradation kinetics
 335 was indeed first order. The value for k_2 ($0.0679 (\frac{1}{hour})$) was derived from
 336 the curve-fit (See further detail in Supplementary Figure S7). Furthermore,
 337 data for the complete chemical reaction were collected by monitoring rhBDNF
 338 concentration over time after placing a predefined amount of PODS®-rhBDNF
 339 into a single well of solution. The data collected appeared to fit the curve for
 340 Equation 2, which describes the concentration of the intermediate product of
 341 two consecutive first order reactions:

$$C_{rhBDNF} = C_{PODS} \cdot k_1 \cdot \left(\frac{e^{-k_1 \cdot t}}{k_2 - k_1} + \frac{e^{-k_2 \cdot t}}{k_1 - k_2} \right) \quad (2)$$

342 where C_{rhBDNF} is the concentration of rhBDNF and C_{PODS} is the concentra-
 343 tion of PODS® [43].

344 We successfully fit the data to this equation's respective curve and empir-
 345 ically approximated k_1 to be $0.00686 (\frac{1}{hour})$ after plugging in our value for k_2
 346 (See further detail in Supplementary Figure S7). Using these calculated rate
 347 constants, the resulting chemical gradient over time after PODS®-rhBDNF
 348 placement can be solved for any geometry by applying Fick's second Law of
 349 diffusion and the appropriate boundary and initial conditions:

$$\frac{dC}{dt} = \nabla \cdot (\nabla C \cdot D) - k_2 \cdot C \quad (3)$$

Boundary conditions:

$$\delta C \Big|_{walls} = 0 \quad (4)$$

350 and

$$\delta C \Big|_{PODS} = k_1 \cdot PODS_0 \cdot e^{-k_1 \cdot t} \quad (5)$$

Initial conditions:

$$C \Big|_{t=0} = 0 \quad (6)$$

351 where C is the concentration of rhBDNF, D is diffusivity of rhBDNF (6.76
352 $\frac{mm^2}{day}$ [44]), $-k_2 \cdot C$ is the sink term corresponding to the degradation and cell-
353 utilization of the rhBDNF. $PODS_0$ is the initial concentration of the cargo
354 protein (i.e., BDNF) within the PODS® crystals. The first boundary condition
355 (Equation 4) shows that the concentrations of rhBDNF at the walls of the
356 microfluidic device are fixed at 0. The second boundary condition (Equation 5)
357 represents the exponential nature of decay of the PODS®. Note that both of
358 them are Neumann boundary conditions.

359 As mentioned, we used the first-order fitted data from our ELISA experi-
360 ment and then determined the values of the $k_{1,2}$ coefficients, which were then
361 applied to the diffusion equation. The finite element model was then computed
362 for different PODS®-rhBDNF concentrations and time intervals to optimize
363 the rhBDNF concentration gradient for hPSC-derived ONP differentiation into
364 SGNs and directed neurite extension. Figure 5 shows FEA-computed rhBDNF
365 concentration gradient for 20,000 PODS®-rhBDNF from Day 1–7. Note that
366 the BDNF concentrations were greater on D2–5 to promote neuronal differentia-
367 tion and neurite outgrowth observed on D7 (Figure 5B). Computed diffusion flux
368 was uniform throughout D1–7 (Figure 5C). Also note that highest concentra-
369 tion of rhBDNF released from PODS®-crystals was greater than 50 pg/mL, the
370 concentration sufficient for otic neuronal differentiation and neurite outgrowth
371 of hPSC-derived ONP 3D spheroids from our previously published data [9].

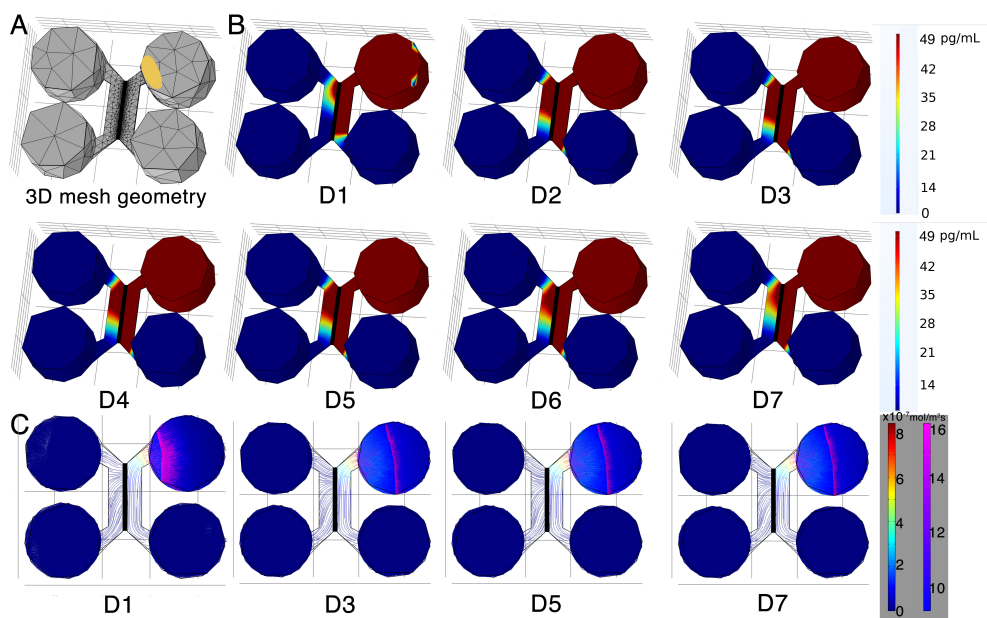


Figure 5: (A): 3D mesh geometry of a Xona™ XC450 created with Autodesk Inventor. An ellipse-shaped PODS®-rhBDNF disc is shown in yellow. (B): Human BDNF concentration gradient for 20,000 PODS®-rhBDNF from D1–D7. Note that the model does not account for media changes during the culture period. The corresponding color map is shown a range from 0 ng/mL to 49 ng/mL. (C): Diffusion flux ($mol/m^2 s$) was computed using COMSOL Chemical Engineering module on D1, D3, D5, and D7.

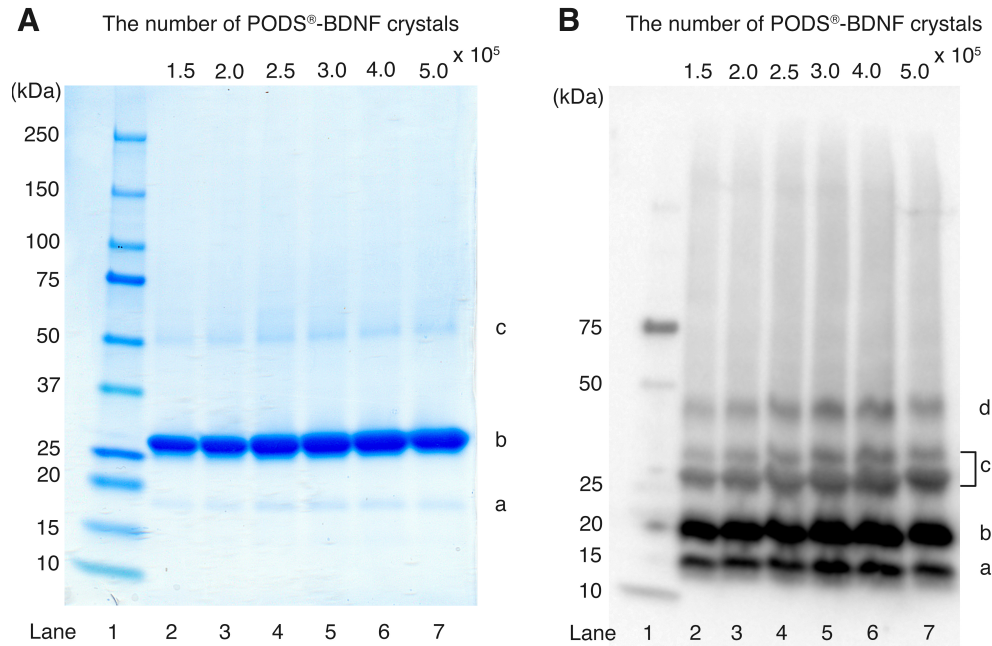


Figure 6: (A): SDS-PAGE analysis of PODS[®]-rhBDNF. Samples containing six quantities of PODS[®]-rhBDNF crystals were run on precast 4-15% polyacrylamide mini-gels and stained with Coomassie G-250 solution for visualization. Protein bands appear at approximately 18.8 (a), 28.0 (b), and 46.8 kDa (c). Lane 1: molecular weight marker. Lanes 2-7: samples containing

372 For the optimization process in determining the adequate number of PODS[®]-
 373 rhBDNF, we also performed FEA with 10,000 and 40,000 PODS[®]-rhBDNF.
 374 Please see detailed discussion of how we determined the optimum concentration
 375 of 20,000 PODS[®]-rhBDNF in Supplementary Figure S8.

376 SDS-PAGE was used to separate PODS[®]-rhBDNF crystals into its con-
 377 stituent proteins to determine the molar ratio of polyhedrin to BDNF. Visu-
 378 alization with Coomassie G-250 solution (Figure 6A) revealed three distinct
 379 protein bands at 18.8 (a), 28.0 (b), and 46.8 (c) kDa, which correspond with
 380 the molecular weights of H1-tagged BDNF monomer, polyhedrin, and H1-tagged
 381 BDNF monomer attached with polyhedrin, respectively. Western blot analy-
 382 sis was subsequently conducted to confirm the identity of the 18.8 kDa band

383 as rhBDNF. Enhanced chemiluminescence (Figure 6B) revealed four protein
384 bands at 14.0 (a), 18.8 (b), 37.6 (c), and 46.8 (d) kDa, which correspond with
385 the molecular weights of rhBDNF monomer, H1-tagged BDNF monomer, H1-
386 tagged BDNF dimer, and H1-tagged BDNF monomer attached with polyhedrin.
387 Immunoblot detection of the 18.8 kDa band further implicates its identity as
388 rhBDNF. SDS-PAGE images were converted to 8-bit grayscale and mean cor-
389 rected integrated pixel intensity values were calculated for protein bands located
390 at 28.0 and 18.8 kDa; the protein band detected at 46.8 kDa was omitted from
391 the final computation based on the notion that it contained a 1:1 ratio of poly-
392 hedrin to BDNF. Results indicate that the molecular ratio of polyhedrin to
393 rhBDNF is approximately 17:1.

394 To objectively compare the degree of otic neuronal differentiation in hPSC-
395 derived ONPs, we performed quantitative analysis of PAX8 and GATA3 double-
396 positive cells using immunocytochemistry. We chose PAX8 and GATA3 for this
397 analysis because our previous studies indicated high expression of these protein
398 markers in late-stage ONPs and early-stage SGNs [8, 9, 24]. Cells were stained in
399 the somal compartment of the Xona™ device, highlighted in green in Figure 7A.
400 Figure 7B shows the resulting image of cells in the somal compartment, and
401 a heat-map representation of the percentage of double-positive cells is shown
402 in Figure 7C. It should be noted here that the heatmap is sensitive to the
403 differences in cell density across channel. This was accounted by averaging
404 the double-positivity across three biological replicates. The heat-map indicates
405 higher double-positivity in the upper region of the somal compartment, which
406 is closest to the PODS®-rhBDNF disc placement (shown in a orange ellipse in
407 Figure 7A) in the neurotrophin compartment. Double-positivity decreases in
408 the somal compartment as distance from the PODS®-rhBDNF disk increases,
409 supporting the presence of a BDNF neurotrophin gradient as predicted by our
410 computational model calculation (Figure 7D).

411 We defined two hypothetical directional angles to predict the orientation of
412 hPSC-derived ONPs and neurite growth (Figure 8). The n -dimensional Eu-
413 clidean space, denoted by \mathbb{R}^n , is a linear vector space in that we can use polar

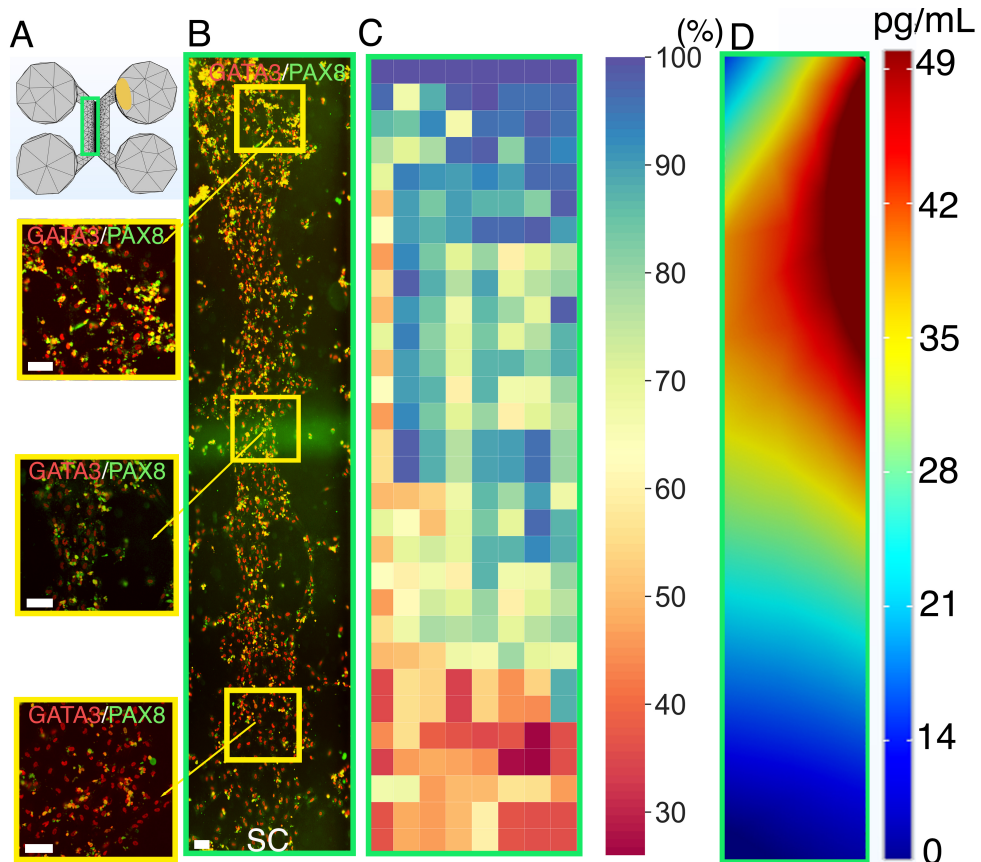


Figure 7: Human PSC-derived late-stage ONPs grown in a microfluidic device at Day 7 were stained for GATA3 (red) and PAX8 (green). (A): Geometry mesh of the microfluidic device Xona™ XC450 generated by Autodesk Inventor. The green square indicates the cell seeding location in the somal compartment of the device. An ellipse-shaped PODS®-rhBDNF disc is shown in yellow. (B): Cells were analyzed by staining with neuronal markers GATA3 (red) and PAX8 (green). Yellow highlighted regions are magnified on the left. SC: somal compartment. (C): Heat-map representation of double-positivity of hPSC-derived ONPs in the device for GATA3 and PAX8 ($n = 3$). Double-positivity increases from the lower to the upper portion of the somal compartment, suggesting that the higher BDNF concentration in the upper portion of the device improves differentiation. Scale bar: 100 μm . (D): Prediction of BDNF concentration gradient released from PODS®-rhBDNF at seven days in culture using a finite element model. The corresponding color map is shown with a range from 0–49 pg/mL.

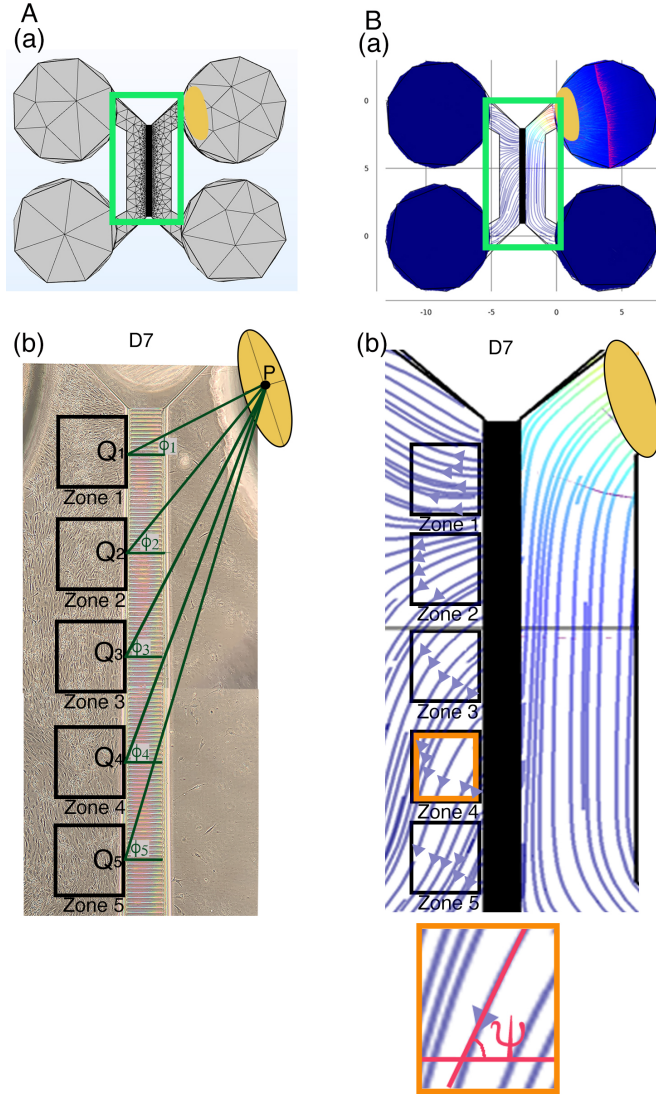


Figure 8: (A): Defining the Euclidean distance angle (EDA). (a) X-Y plane geometry mesh of a Xona™ XC450 device. Green square shows an area corresponding to a phase-contrast image below. An ellipse-shaped PODS®-rhBDNF disc is shown in yellow. (b) hPSC-derived ONPs were cultured in a Xona™ XC450 for seven days (D7). Yellow ellipse once again indicates the location of a disk contains PODS®-rhBDNF crystals (P: the center of this ellipse). In the somal compartment of the Xona™ XC450 device, we defined Zone 1–5, shown in black square. A line was drawn from the center of the PODS®-rhBDNF disk (P) to (Q_{1–5}) (i.e., the near side to microgroove channels) of a pre-designated square (shown as a black square, zone 1–5) [i.e.,zone 1–5]. The Euclidean distance angle (EDA) for zone 1–5 was defined as ϕ_i , $i = 1–5$. (B): Defining diffusion flux angle (DFA). (a) Diffusion flux in a Xona™ XC450. Green squared area show a somal and neurotrophin compartment, which are magnified in (b). (b) Magnified image of diffusion flux of Zone 1–5 in a Xona™ XC450. Orange highlighted zone (zone 4) was magnified at the bottom of (b), defining a DFA (ψ).

414 coordinates to compute the directionality of cells and neurites [45]. Here, we
415 used $n = 1$ and 2. For one-dimensional Euclidean space ($n = 1$), we simply drew
416 a line for the Euclidean distance—the shortest distance between two points as
417 shown in Figure 8A(b) (dark green lines). The two points were 1) the center
418 point of a PODS®-rhBDNF disk (P) and 2) the mid point of the medial side
419 (i.e., the near side to microgroove channels) of a pre-designated square
420 (shown as a black square, zone 1–5 in Figure 8), respectively. The Euclidean
421 distance angle (EDA), ϕ_i , was defined as the angle between the horizontal line
422 zero direction and the line PQ_i that consists of the Euclidean distance where i
423 = 1–5.

424 For two-dimensional Euclidean space ($n = 2$), we utilized Fick’s first law,
425 which dictates that the diffusion flux (D) is proportional to the concentration
426 gradient (C) [46]. Based on this theorem, the direction of a flow vector can
427 be used to represent concentration gradient for the directionality. We hypothe-
428 sized here that cell orientation is directionally controlled by the flux vector
429 which is driven by the concentration gradient. Figure 8B shows the flow vectors
430 in a somal compartment at Day 7 computed by COMSOL Chemical engineering
431 module. We averaged the 10 flow vectors in each of five zones in Figure 8 to
432 compute diffusion flux angle (DFA), ψ_i , where $i = 1–5$ in Figure 8. To lighten
433 the computational intensity, we reduced a dimension from 3D to 2D to com-
434 pute diffusion Flux. Please see justification in Supplementary Data. All of the
435 computed EDAs and DFAs can be found in Supplementary Table 2.

436 Figure 9 shows time-series of microscopic phase-contrast photomicrographs
437 obtained on Day 1, 3, and 7 in the five zones in a Xona™ XC450. Each preferred
438 orientation of any given cell was computed and then plotted on a polar diagram
439 (blue circle). Mean vector angle (MVA, shown in red line on Figure 9) and
440 median vector angle were computed. All of the polar diagrams in Figure 9 show
441 that preferred orientation of hPSC-derived ONPs distribute in an unimodal dis-
442 tribution. We also confirmed that a von Mises distribution is appropriate for
443 these sets of data (See Supplementary Figure S9). We, therefore, then tested
444 further to see if the cells had tendency to be oriented to a certain direction.

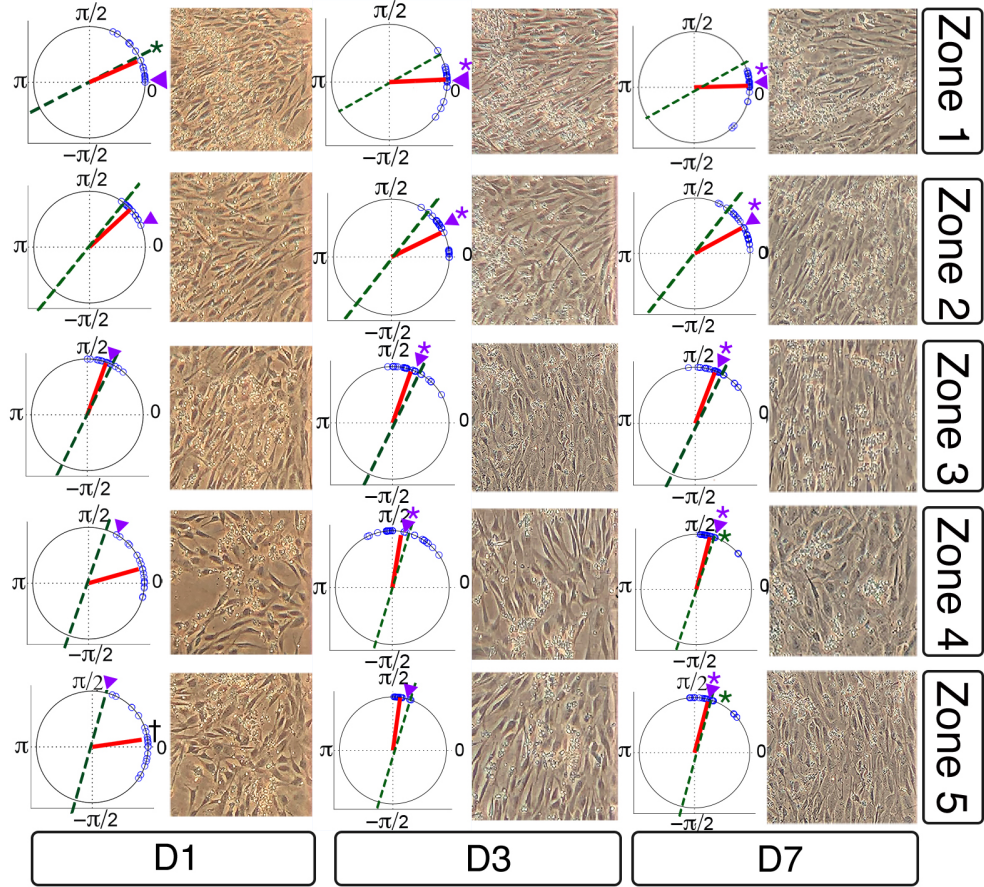


Figure 9: Preferred cell orientation analysis. Sequential phase-contrast images of a somal compartment of a Xona™ XC450 device in zone 1–5 (see Figure 8) on day 1 (D1), day 3 (D3), and day 7 (D7). A corresponding polar histogram indicates preferred orientation of hPSC-derived ONPs in an angle (0 – 2π radians) in blue circles. Mean vector angle is shown in red line. Green dotted line shows Euclidean Distance Angle (EDA) and purple triangle indicates Diffusion Flow Angle (DFA). † symbol indicates that p value > 0.01 . * symbol indicates that the mean vector angle fits within the 95% confidence internal ($\alpha < 0.05$.)

445 To test this hypothesis, we used the Rayleigh test of uniformity to evaluate
446 whether there is statistical evidence of circular directionality [32]. Computed
447 p values for all the 15 conditions were less than 0.05, demonstrating that all
448 of the conditions had statistically significant directionality. To further validate
449 whether the observed angles have a tendency to cluster around the two hypo-
450 thetical angles (i.e., EDA and DFA), we then performed the V test. Once again,
451 p values for all 15 conditions were less than 0.05 except one (Zone 5 on Day 1),
452 re-demonstrating that most of the conditions had statistically significant ten-
453 dencies to cluster around the EDAs and DFAs. Finally, to investigate whether
454 the preferred orientation of the cells were clustered around the EDAs or DFAs,
455 we performed one sample test for the mean vector angle, which is similar to a
456 one sample t-test on a linear scale. There was only one condition (Zone 1, day
457 1) that was statistically significant for EDA, whereas most of the conditions on
458 Day 3 and 7 were statistically significant for DFA. Therefore, our results here
459 demonstrated that hPSC-derived ONPs had greater tendency to cluster around
460 DFA than EDA. All computed statistical values are shown in Supplementary
461 Table S2.

462 To evaluate the direction of neurites of hPSC-derived ONPs, we first de-
463 fined EDA in Region 1-3 (ϕ'_j , $j = 1 - 3$) (Figure 10A) and DFA (ψ'_j , $j = 1-3$);
464 similarly defined ϕ_i and ψ_i as in Figure 8. All of the EDAs and DFAs defined
465 here can be found in Supplementary Table S3. Polar histograms of the neurite
466 direction angle in Region 1–3 indicated that the two longest neurites were bi-
467 modal in nature (Figure 10B). In contrast, polar histograms of those cultured
468 with rhBDNF (negative control) and 800,000 PODS®-BNDF (positive control)
469 did not indicate bimodal distribution—the neurites did not show directionality
470 (Figure 10C). The Rayleigh test of uniformity for both the positive and negative
471 control were greater than 0.05, demonstrating that both of the conditions had
472 no statistically significant directionality (Supplementary Table S3: highlighted
473 in green). We also analyzed the direction of the neurites using circular statistics.
474 To obtain more realistic mean vector angles, we doubled each angle and reduced
475 the multiples modulo 360°. In circular statistics, the bimodal distributed data

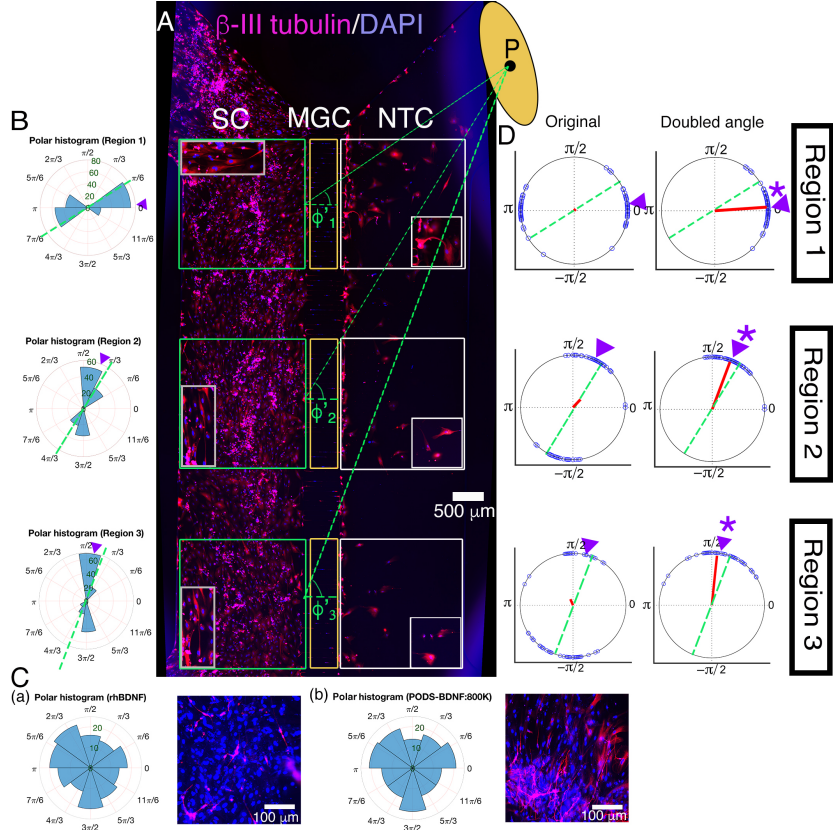


Figure 10: (A): Immunohistochemistry of hPSC-derived ONPs cultured in the Xona™ XC450 for seven days with β -III-Tubulin (pink fluorescence) and DAPI (blue fluorescence). A green line was drawn from the center of the BDNF disk (P) to the mid point of each of three pre-determined squares (Region 1–3) in the somal compartment to define Euclidean Distance Angle (EDA: ϕ_i^c , $i = 1 - 3$). Green square: somal compartment (SC); yellow square: microgroove channels (MGC); White square: Neurotrophin compartment (NTC). High-power magnified images of the NTC and SC are shown. An ellipse-shaped PODS®-rhBDNF disc is shown in yellow. P: the center of the disk.(B): Polar histogram of neurite directional angles of hPSC-derived ONPs in the Xona™ XC450 at Day 7 (D7). The two longest neurites were measured. EDA: green dotted line. DFA: purple triangle. (C): (a) Right: Polar histogram of neurite directional angles of hPSC-derived ONPs cultured with 20 ng/mL of recombinant human BDNF for seven days. Left: Corresponding photomicrograph of immunocytochemistry with β -III tubulin (pink) and DAPI (blue). (b) Right: Polar histogram of neurite directional angles of hPSC-derived ONPs cultured with 800,000 of PODS®-rhBDNF for seven days. Left: Corresponding photomicrograph of immunocytochemistry with β -III tubulin (pink) and DAPI (blue). (D): A circular plot of neurite directional angle of hPSC-derived ONPs in Region 1–3. Once again, the two longest neurites were plotted on a unit circle. Right column: Original directional angle distribution. Left column: the method of doubling the angle applied to the original data. Each datum point is shown as a blue circle. Mean vector angle is shown as a red line. Green dotted line shows Euclidean Distance Angle (EDA) and purple triangle indicates Diffusion Flow Angle (DFA). * symbol indicates that the mean vector angle fits within the 95% confidence internal ($\alpha < 0.05$.)

476 can be transformed into a unimodal data by doubling the angle [32]. The mean
477 vector angles in Figure 10D (right column) indicates the situation where the
478 vectors were canceled out between the two groups of angles distributed in a bi-
479 modal fashion, resulting in inaccurate representation. A circular plot in Figure
480 10D (right column) showed doubled angles, representing actual representation
481 of the neurite vector angles. In all of the three regions, the Reyleigh test and V
482 test for EDA and DFA indicated directionality (Supplementary Table S3). One
483 sample test for the mean vector angles in Region 1–3 indicated that they were
484 not statistically different from DFA, but all of the three mean vector angles were
485 statistically different from EDA.

486 We also stained the devices for β -III tubulin to track neurite growth and
487 extension across the micro-groove channels as well as cell migration in three
488 selected regions (Figure 10A). The location of the PODS®-rhBDNF disk in
489 relation to the regions of interest in Figure 11A is indicated by a yellow circle.
490 Quantitative analyses were performed and summarized in Figure 11B. Our data
491 indicate that neurite length is dependent on BDNF concentration, with greater
492 amounts of PODS®-rhBDNF promoting longer neurite growth (Figure 11B(a)).
493 Lesser amounts of PODS®-rhBDNF, however, are necessary to create an ap-
494 propriate concentration gradient. In the presence of 20,000 PODS®-rhBDNF,
495 both neurite extension into the microchannels and cell migration into the neu-
496 rotrophin compartment are greatest in the region closest to the BDNF source
497 and decrease further from the PODS®-rhBDNF (Figure 11B(b,c)). Cell migra-
498 tion is dependent on the distance from the source of BDNF, thus suggesting the
499 presence of a BDNF gradient as predicted by our model. Note that the Xona
500 microchannels intended to prevent from migration across channels.

501 **4. Discussion**

502 *4.1. Challenges in neurotrophin treatment in the inner ear*

503 This is a proof-of-concept study for the realization of a neurotrophic strip
504 to ascertain its scientific/technological parameters in a controlled *in vitro* en-

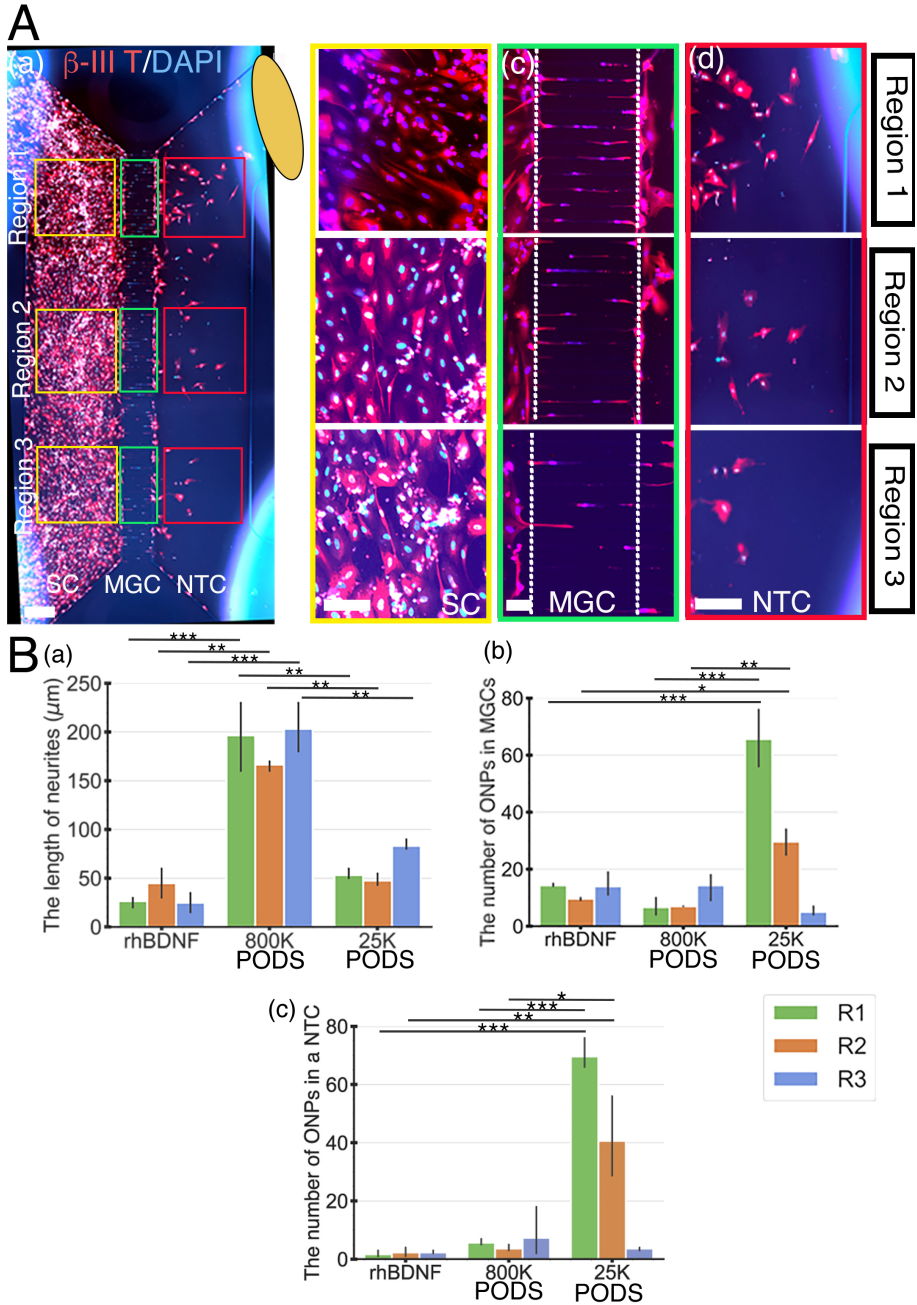


Figure 11: Human PSC-derived late-stage ONPs in the microfluidic device were stained with β -III tubulin (red) and DAPI (blue) to measure cell migration. (A): Late-stage ONPs stained after seven days in culture (a) with regions highlighted and magnified in the somal compartment (b), microgroove channels (c), and neurotrophin compartment (d). SC: somal compartment, MGC: microgroove channels, NTC: neurotrophic compartment. An ellipse-shaped PODS®-rhBDNF disc is shown in yellow. Scale bar (a): 500 μm ; (b)–(d): 100 μm . (B): Quantitative analyses of cell migration and neurite extension in devices using recombinant human BDNF, 800,000 PODS®-rhBDNF, or 20,000 PODS®-rhBDNF. * : $p < 0.05$, **: $p < 0.01$, ***: $p < 0.001$.

505 vironment. Neurotrophin gradients have been studied for in multiple contexts
506 [47, 48, 49]. However, it has not been feasible to reliably provide such a gra-
507 dient to neurons neither *in vitro* nor *in vivo*, primarily because of technical
508 challenges. While neurotrophin treatment has been recognized as a potential
509 treatment for sensorineural hearing loss, there has not been clinical success in
510 this avenue to date. Most recent relevant clinical trials used adeno-associated
511 virus (AAV2) to deliver BDNF to the brain [50]. Although exciting, this treat-
512 ment does not attempt to control the concentration of BDNF, which could
513 potentially interfere with normal functions in a target organ [51]. Furthermore,
514 this treatment may not be applicable to the inner ear. In this study, we used
515 PODS®-rhBDNF to provide a neurotrophic gradient in a controlled fashion.
516 Our result indicated 20,000 PODS-BDNF allowed for rhBDNF neurotrophin
517 gradient such that hESC-derived ONPs survived, differentiated toward human
518 SGNs, and also established directional neurite outgrowth in a microfluidic device.

519 *4.2. Microfluidic device-generated gradient*

520 We used a microfluidic device to advance our understanding of directional
521 neurite growth and otic neuronal differentiation in response to a BDNF concen-
522 tration gradient [52]. Among many *in vitro* concentration gradient sustaining
523 culture devices, microfluidic devices have overcome many of the deficits that
524 conventional platforms (i.e., the Boyden chamber, Dunn chambers, or compart-
525 mentalized diffusion chambers) face [52]. Conventional platforms tend to be sub-
526 optimal to manipulate small volumes of fluid at the order of microliters. Growth
527 factors and proteins are used in minute amounts in our microfluidic device, and
528 cultured stem cells are able to interact with endogenous factors. As mentioned
529 earlier, this micro-environment more accurately represents *in vivo* conditions.
530 The Xona™ device can be used to sustain a three-dimensional concentration gra-
531 dient over time (duration dependent on the half-life of the molecule) due to its
532 microchannel array. The device limits convective flow in the gradient-forming
533 areas by introducing microgroove channels that generate high fluidic resistance,
534 thereby limiting flow to diffusion. The high resistance of the microchannel array

535 also prolongs diffusion across them, thereby increasing both gradient formation
536 and gradient steepness. These features allowed us to generate a FEM, which pre-
537 dicted the necessary number of PODS®-BDNF crystals for a BDNF gradient.
538 Note, however, that this environment is different from the micro environment
539 in the inner ear. A mesh geometry of the cochlea will be needed to compute the
540 PODS®-BDNF crystal number for our next step of this study.

541 *4.3. BDNF and Polyhedrin protein*

542 Over the course of past 20–30 years, it has been established that BDNF me-
543 diates survival and differentiation activities on SGNs by binding and activating
544 the tyrosine kinase receptor kinase B (TrkB), a member of the larger family
545 of Trk receptors [20]. Numerous studies have reported that BDNF can palliate
546 SGN degeneration in ototoxically deafened animals, a widely accepted model for
547 retrograde trans-synaptic SGN degeneration secondary to hair cell destruction
548 [13, 14, 53, 54]. Additionally, it has been confirmed that there is a positive corre-
549 lation between SGN counts and CI performance [55]. It is then safe to presume
550 that treating CI recipients with BDNF would enhance overall CI performance,
551 by preserving SGNs and their neurites. However, simply introducing rhBDNF
552 into the inner ear poses significant hurdles. Although promising, human BDNF
553 treatment has not been currently implemented in the inner ear. Unsuccessful
554 BDNF treatment can be explained by several factors [56].

555 The blood half-life of BDNF protein is extremely short, only 1–10 min in
556 the plasma [57, 58] and one hour in CSF [59]. The BDNF’s high degrada-
557 tion rate would require continuous replenishment, impractical for clinical use.
558 Furthermore, introduction of a homogeneous solution of BDNF would promote
559 nondirectional neurite growth where directed neurite growth is essential for de-
560 signing our new-generation bioactive CI, as depicted in Figure 1A. Directing
561 neurite growth towards the CI electrode array is pivotal in the ultimate goal
562 of enhancing performance through the narrowing of the electrode-neuron gap.
563 The PODS® system precludes the phenomena by its localized, gradual release
564 of growth factor. The steady supply of BDNF from a localized origin not only

565 creates a concentration gradient, but maintains it over time. As seen in Figures
566 4–6, we were able to perform a finite element analysis based on data we collected
567 describing the chemical release kinetics and molar ratio of PODS®-BDNF sys-
568 tem. It is clearly visible that the slow-release nature of PODS®-BDNF results
569 in a concentration gradient over the course of Day 1–7 (Figure 5).

570 It should be noted that our FEM assumes free diffusion of the rhBDNF
571 protein. In biological cell-culture conditions, BDNF released from PODS®-
572 BDNF has tendency to adhere to the walls of the culture device because BDNF
573 is a “sticky” protein of about 27 kDa (mature BDNF dimer) and it is positively
574 charged under physiological conditions (isoelectric point, pI = 9.4) [60]. As such,
575 the physio-chemical properties of BDNF have made the recombinant protein
576 difficult to diffuse. This phenomenon was observable in preliminary data where
577 the ONPs failed to survive past 1–3 days of culture (data not shown). To
578 circumvent this issue we infused the culture media with a carrier protein (i.e.,
579 BSA), hypothesizing that the albumin would act as a carrier for the released
580 BDNF and allow for free diffusion throughout the microfluidic device [61]. This
581 hypothesis is supported by our sets of biological verification data (Figures 7–11)
582 that clearly shows that hPSC-derived ONPs responded to the modification by
583 exhibiting the expected cell body orientation, unidirectional neurite extension,
584 and neurite length. Note that albumin is the single protein found in highest
585 concentrations in the perilymph [62], therefore, a carrier protein will not be
586 needed in our future *in vivo* study.

587 *4.4. Intracellular signaling initiated by Thyrosine kinase B receptor*

588 Another issue we need to consider in interpretation of our results is the intra-
589 cellular cell signaling mechanism elicited by rhBDNF. Human BDNF (mature
590 dimeric form) binds with high affinity to its TrkB receptor. The binding of
591 BDNF to a TrkB receptor has proven to have significant importance for the
592 proneuronal effects of BDNF [20]. Upon binding BDNF, TrkB dimerizes, and
593 activates intrinsic kinase activities and other complex set of intracellular sig-
594 naling cascades, which is beyond the scope of this study. However, it should

595 be noted that activation of TrkB receptor by neurotrophin binding causes the
596 TrkB protein to be internalized in endosomes on the cellular membrane [63].
597 Endosomes can then be transported to the soma. Therefore, the proneuronal
598 effects of rhBDNF in our results might have highly depended on the status of
599 TrkB receptors on the cell membrane of hPSC-derived ONPs. Our previous
600 study has demonstrated that strong expression of a TrkB receptor on derived
601 ONPs [24], however, more detailed studies on TrkB receptors on hPSC-derived
602 ONP and SGNs will be needed.

603 *4.5. Degradation of PODS® crystals by protease*

604 In cell culture, degradation of PODS®-rhBDNF is likely due to the activity
605 of cell-secreted proteases. The proteases break down the peptide bonds of the
606 encasing polyhedrin protein, creating openings in the structure to allow release
607 of the rhBDNF. Therefore, the presence of proteases is imperative for the proper
608 utilization of the PODS® crystals. Additionally, these proteases are responsible
609 for the degradation of the released BDNF. Because stem cells are not present
610 in the culture media used for the PODS® degradation kinetics experiments, we
611 infused the media with 10% FBS, which naturally contains proteases, to promote
612 polyhedrin degradation, BDNF release, and BDNF degradation to attain results
613 that more accurately describe *in vitro* events. Moreover, since the cells and
614 PODS are initially segregated into separate compartments within the culture
615 device, cell-secreted proteases are unlikely to reach and degrade the PODS in
616 time to support ONP survival and differentiation. Infusion of FBS was therefore
617 required in these experiments as well. In clinical use, however, we presume
618 that cell-secreted proteases will be readily present in the inner ear and would
619 therefore preclude the need for artificial supplementation.

620 *4.6. A concept design: Neurotrophic strip*

621 The plateau in CI performance in treatment of sensorineural hearing loss has
622 driven researchers to develop innovative supplementary treatment strategies to
623 push the field past this hurdle. Our approach strives to directly address the

624 issue at its core: the electrode-neuron gap, which can lead to serious implica-
625 tions include low spatial frequency resolution and high power consumption. We
626 can use our data as a launchpad for the neurotrophic strip (NS). The NS is a
627 biointerface concept that integrates an extended-release source of growth factor
628 to facilitate a protein gradient. Implanted in conjunction with the CI, it acts
629 as a bridge between the extant SGNs and implanted late-ONPs grown on the
630 electrode itself. The NS would promote survival of both cell populations, dif-
631 ferentiation of the late ONP implants, promote directional neurite growth and
632 synaptogenesis between the two, effectively creating a neuronal network between
633 the patient and the implanted CI. Each electrode would be able to stimulate cell
634 bodies at exceptionally high resolution, essential for greater intonation differ-
635 entiability (required for effective social interaction and music appreciation) and
636 so, increased quality of life for millions. Our successful outcomes are essential
637 to make a neurotrophic strip feasible in *in vivo* environment.

638 *4.7. The limitations of this study and future direction*

639 There are some limitations associated with this study. First, the reduction of
640 spacial dimension to 2D for diffusion modeling certainly affected the flux vector,
641 which determines the predicted concentration vector. Given that the thickness
642 (i.e., Z-axis) of the microfluidic device was 100 μm , we estimated that the effect
643 was minimal. In the future, we plan to use PSC-derived 3D spheroids in a somal
644 compartment so that flux vector and concentration gradient vector can more
645 accurately model the cell behavior. In this way, we will be able to circumvent
646 the need to reduce diffusion calculations to 2D for computation performance in
647 the modeling.

648 Secondly, we required to generate a model in that the BDNF's biological
649 transportation phenomenon from a PODS®-rhBDNF disk to a somal compart-
650 ment of a Xona™ device. Note that in this model, we focused on the major
651 dependent variable, BDNF concentration gradient to model the biological phe-
652 nomenon. Other physical variables to promote cell migration, otic neuronal
653 differentiation, and neurite growth were not take into consideration. These

654 variables include electotaxis (electrical potential), durotaxis (matrix's stiffness
655 [i.e., laminin 511 in our case]) [64], mechanotaxis (cell strain), and lastly cell
656 migration by random walk [65]. In our future study, we will take these vari-
657 ables into consideration to more accurately represent the migration and neurite
658 growth of hPSC-derived ONPs.

659 Insufficient contrast between cells and background in phase contrast images
660 led to inaccuracies in cell orientation computation for some images. To address
661 this issue, poor quality images were disregarded in the quantitative analysis.
662 We occasionally used manual measurement for accuracy. Our future study may
663 entail automated time-series cell analysis, which would allow more accurate
664 measurement. Also, another way to address this issue would be with a cell
665 membrane staining in the future.

666 While 20,000 of PODS®-rhBDNF were necessary for hPSC-derived ONPs
667 for otic neuronal differentiation and directional neurite outgrowth, this condi-
668 tion may not be sufficient. For instance, it is still not known whether the effects
669 of other neurotrophic factors such as Neurotrophin-3 and Glial cell line-derived
670 neurotrophic factor could have a positive effect on ONP growth [20, 66, 67]. We
671 are planning to investigate these neurotrophic factors in the future. Other fac-
672 tors that could have an impact on directional neurite growth include endogenous
673 factors secreted from hPSC-derived ONPs. While our previous study demon-
674 strated that hPSC-derived ONPs only secreted negligible amount of BDNF that
675 were detected by ELISA [9], currently we do not have any data on other neu-
676 rotrophic factors or other molecules that could have affected directional neurite
677 growth in the inner ear. We chose BDNF first to study because the most inten-
678 sively studied neurotrophic factor in the field of hearing research is BDNF [20].
679 Previous studies have indicated that neurotrophic supports of SGNs are mainly
680 from BDNF and neurotrophin-3 (NT-3) [20, 60]. Therefore, the potential con-
681 founding effect of the secretions of other neurotrophic factors and molecules
682 secreted from derived SGNs are likely NT-3, for which further investigation is
683 necessary in the future.

684 Despite the aforementioned limitations associated in this study, the present

685 results generated BDNF concentration gradient, condition of which is necessary
686 for hPSC-derived ONPs to differentiate into the otic lineage (i.e., SGNs) and
687 also promoted directional neurite extension towards the POD-BDNF disk. The
688 technique will allow us to control neurite direction of transplanted hPSC-derived
689 ONPs in the inner ear. We will harness this method in our design of a bioactive
690 CI.

691 **Conclusions**

692 We were able to generate BDNF concentration gradient, enabling survival,
693 neuronal differentiation toward SGNs, and directed neurite extension of hPSC-
694 derived ONPs. The technique will allow us to control neurite direction of trans-
695 planted hPSC-derived ONPs in the inner ear. This proof-of-concept study pro-
696 vides a step toward next-generation bioacitve CI technology.

697 **Acknowledgment**

698 This work was supported by the American Otological Society Clinician Sci-
699 entist Award (AJM), the Triological Society/American College of Surgeons
700 Clinician Scientist Award (AJM), the Department of Otolaryngology of North-
701 western University (AJM), the NIH (NIDCD) K08 Clinician Scientist Award
702 K08DC13829-02 (AJM), and the Office of the Assistant Secretary of Defense of
703 Health Affairs through the Hearing Restoration Research Program (Award #:
704 RH170013:WU81XWUH-18-0712). Imaging work was performed at the North-
705 western University Center for Advanced Microscopy, which is generously sup-
706 ported by NCI CCSG P30 CA060553 awarded to the Robert H. Lurie Com-
707 prehensive Cancer Center, for which we thank Peter Dluhy, Constadina Ar-
708 vanitis, Ph.D., David Kirchenbuechler, Ph.D., and Wensheng (Wilson) Liu,
709 M.D. Some of microfluidic device experiments were performed in the Analytical
710 bioNanoTechnology (ANTEC) Core Facility of the Simpson Querrey Institute
711 at Northwestern University, which is supported by the Soft and Hybrid Nan-
712 otechnology Experimental (SHyNE) Resource (NSFECCS-1542205). We thank

713 Shreyas Bharadwaj (Cornell University), Kyle Coots (Midwestern University),
714 Andrew Oleksijew (the University of Nebraska), Duncan Chadly (California In-
715 stitute of Technology), and Shun Kobayashi (the University of Texas at Austin)
716 for their contribution to the earlier phases of this project. We thank Sara Dun-
717 lop (Department of Neurology, Northwestern University), and Dr. Jacqueline
718 Bond (the University of California San Diego) for assistance in Western Blot and
719 SDS-Page gels. We also thank Dr. Georgia Minakaki (Department of Neurol-
720 ogy, Northwestern University) on assistance in ELISA. Finally, our thanks and
721 appreciation go to our collaborator, Dr. Christian Pernstich (Cell Guidance
722 Systems), for continuous support and stimulating discussions on this project
723 since 2015.

724 **References**

- 725 [1] J. G. Naples, M. J. Ruckenstein, Cochlear Implant., Otolaryngologic Clinics
726 of North America 53 (1) (2020) 87–102. doi:10.1016/j.otc.2019.09.
727 004.
- 728 [2] B. S. Wilson, M. F. Dorman, Cochlear implants: A remarkable past
729 and a brilliant future, Hearing Research 242 (1-2) (2008) 3–21. arXiv:
730 NIHMS150003, doi:10.1016/j.heares.2008.06.005.
- 731 [3] C. Frick, M. Müller, U. Wank, A. Tropitzsch, B. Kramer, P. Senn, H. Rask-
732 Anderson, K. H. Wiesmüller, H. Löwenheim, Biofunctionalized peptide-
733 based hydrogels provide permissive scaffolds to attract neurite outgrowth
734 from spiral ganglion neurons, Colloids and Surfaces B: Biointerfaces 149
735 (2017) 105–114. doi:10.1016/j.colsurfb.2016.10.003.
- 736 [4] S. Hahnewald, A. Tscherter, E. Marconi, J. Streit, H. R. Widmer, C. Gar-
737 nham, H. Benav, M. Mueller, H. Löwenheim, M. Roccio, P. Senn, Response
738 profiles of murine spiral ganglion neurons on multi-electrode arrays., Jour-
739 nal of neural engineering 13 (1) (2016) 16011. doi:10.1088/1741-2560/
740 13/1/016011.

- 741 [5] R. K. Shepherd, S. Hatsushika, G. M. Clark, Electrical stimulation of
742 the auditory nerve: The effect of electrode position on neural excitation,
743 Hearing Research 66 (1) (1993) 108–120. doi:10.1016/0378-5955(93)
744 90265-3.
- 745 [6] M. Tykocinski, L. T. Cohen, B. C. Pyman, T. Roland, C. Treaba, J. Palamara,
746 M. C. Dahm, R. K. Shepherd, J. Xu, R. S. Cowan, N. L. Cohen,
747 G. M. Clark, Comparison of electrode position in the human cochlea using
748 various perimodiolar electrode arrays., The American journal of otology
749 21 (2) (2000) 205–211. doi:10.1016/S0196-0709(00)80010-1.
- 750 [7] A. Roemer, U. Köhl, O. Majdani, S. Klöß, C. Falk, S. Haumann, T. Lenarz,
751 A. Kral, A. Warnecke, Biohybrid cochlear implants in human neurosensory
752 restoration., Stem cell research and therapy 7 (1) (2016) 148. doi:10.
753 1186/s13287-016-0408-y.
- 754 [8] R. A. Heuer, K. T. Nella, H. T. Chang, K. S. Coots, A. M. Oleksijew,
755 C. B. Roque, L. H. Silva, T. L. McGuire, K. Homma, A. J. Matsuoka,
756 Three-dimensional otic neuronal progenitor spheroids derived from human
757 embryonic stem cells, Tissue Engineering - Part A 27 (3-4) (2021) 256–269.
758 doi:10.1089/ten.tea.2020.0078.
- 759 [9] H.-T. Chang, R. A. Heuer, A. M. Oleksijew, K. S. Coots, C. B. Roque, K. T.
760 Nella, T. L. McGuire, A. J. Matsuoka, An Engineered Three-Dimensional
761 Stem Cell Niche in the Inner Ear by Applying a Nanofibrillar Cellulose
762 Hydrogel with a Sustained-Release Neurotrophic Factor Delivery System,
763 Acta Biomaterialia 108 (2020) 111–127. doi:<https://doi.org/10.1016/j.actbio.2020.03.007>.
- 764 [10] L. Taylor, L. Jones, M. H. Tuszyński, A. Blesch, Neurotrophin-3 gradients
765 established by lentiviral gene delivery promote short-distance axonal bridg-
766 ing beyond cellular grafts in the injured spinal cord, Journal of Neuroscience
767 26 (38) (2006) 9713–9721. doi:10.1523/JNEUROSCI.0734-06.2006.

- 769 [11] P. Senn, M. Roccio, S. Hahnewald, C. Frick, M. Kwiatkowska, M. Ishikawa,
770 P. Bako, H. Li, F. Edin, W. Liu, H. Rask-Andersen, I. Pyykkö, J. Zou,
771 M. Mannerström, H. Keppner, A. Homsy, E. Laux, M. Llera, J. P. Lel-
772 louche, S. Ostrovsky, E. Banin, A. Gedanken, N. Perkas, U. Wank, K. H.
773 Wiesmüller, P. Mistrík, H. Benav, C. Garnham, C. Jolly, F. Gander, P. Ul-
774 rich, M. Müller, H. Löwenheim, NANOCI-Nanotechnology Based Cochlear
775 Implant with Gapless Interface to Auditory Neurons, *Otology and Neuro-*
776 *urology* 38 (8) (2017) e224—e231. doi:10.1097/MAO.0000000000001439.
- 777 [12] G. J. Goodhill, H. Baier, Axon Guidance: Stretching Gradients to
778 the Limit, *Neural Computation* 10 (3) (1998) 521–527. doi:10.1162/
779 089976698300017638.
- 780 [13] L. N. Gillespie, G. M. Clark, P. F. Bartlett, P. L. Marzella, BDNF-induced
781 survival of auditory neurons *in vivo*: Cessation of treatment leads to ac-
782 celerated loss of survival effects, *Journal of Neuroscience Research* 71 (6)
783 (2003) 785–790. doi:10.1002/jnr.10542.
- 784 [14] L. N. Pettingill, R. L. Minter, R. K. Shepherd, Schwann cells geneti-
785 cally modified to express neurotrophins promote spiral ganglion neuron
786 survival *in vitro*, *Neuroscience* 152 (3) (2008) 821–828. doi:10.1016/j.
787 *neuroscience*.2007.11.057.Schwann.
- 788 [15] R. K. Shepherd, A. Coco, S. B. Epp, Neurotrophins and electrical stim-
789 ulation for protection and repair of spiral ganglion neurons following
790 sensorineural hearing loss, *Hearing Research* 242 (2009) 100–109. doi:
791 10.1016/j.heares.2007.12.005.Neurotrophins.
- 792 [16] B. Baseri, J. J. Choi, T. Deffieux, G. Samiotaki, Y. S. Tung, O. Olu-
793 molade, S. A. Small, B. Morrison, E. E. Konofagou, Activation of sig-
794 naling pathways following localized delivery of systemically administered
795 neurotrophic factors across the bloodbrain barrier using focused ultra-
796 sound and microbubbles, *Physics in Medicine and Biology* 57 (7). doi:
797 10.1088/0031-9155/57/7/N65.

- 798 [17] K. Ikeda, S. Nagaoka, S. Winkler, K. Kotani, H. Yagi, K. Nakanishi,
799 S. Miyajima, J. Kobayashi, H. Mori, Molecular Characterization of Bom-
800 byx mori Cytoplasmic Polyhedrosis Virus Genome Segment 4, *Journal of*
801 *Virology* 75 (2) (2001) 988–995. doi:[10.1128/jvi.75.2.988-995.2001](https://doi.org/10.1128/jvi.75.2.988-995.2001).
- 802 [18] T. Suzuki, T. Kanaya, H. Okazaki, K. Ogawa, A. Usami, H. Watanabe,
803 K. Kadono-Okuda, M. Yamakawa, H. Sato, H. Mori, S. Takahashi, K. Oda,
804 Efficient protein production using a Bombyx mori nuclear polyhedrosis
805 virus lacking the cysteine proteinase gene, *Journal of General Virology*
806 78 (12) (1997) 3073–3080. doi:[10.1099/0022-1317-78-12-3073](https://doi.org/10.1099/0022-1317-78-12-3073).
- 807 [19] H. Mori, R. Ito, H. Nakazawa, M. Sumida, F. Matsubara, Y. Minobe,
808 Expression of Bombyx mori cytoplasmic polyhedrosis virus polyhedrin in
809 insect cells by using a baculovirus expression vector, and its assembly into
810 polyhedra, *Journal of General Virology* 74 (1) (1993) 99–102. doi:[10.1099/0022-1317-74-1-99](https://doi.org/10.1099/0022-1317-74-1-99).
- 812 [20] S. H. Green, E. Bailey, Q. Wang, R. L. Davis, The Trk A, B, C's of
813 Neurotrophins in the Cochlea., *Anatomical record* (Hoboken, N.J. : 2007)
814 295 (11) (2012) 1877–1895. doi:[10.1002/ar.22587](https://doi.org/10.1002/ar.22587).
- 815 [21] I. Meyvantsson, D. J. Beebe, Cell culture models in microfluidic systems,
816 *Annual Review of Analytical Chemistry* 1 (1) (2008) 423–449. doi:[10.1146/annurev.anchem.1.031207.113042](https://doi.org/10.1146/annurev.anchem.1.031207.113042).
- 818 [22] Z.-J. Guo, M.-H. Yu, X.-Y. Dong, W.-L. Wang, T. Tian, X.-Y. Yu, X.-D.
819 Tang, Protein composition analysis of polyhedra matrix of Bombyx mori
820 nucleopolyhedrovirus (BmNPV) showed powerful capacity of polyhedra to
821 encapsulate foreign proteins., *Scientific reports* 7 (1) (2017) 8768. doi:
822 [10.1038/s41598-017-08987-8](https://doi.org/10.1038/s41598-017-08987-8).
- 823 [23] A. J. Matsuoka, Z. A. Sayed, N. Stephanopoulos, E. J. Berns, A. R. Wad-
824 hwani, Z. D. Morrissey, D. M. Chadly, S. Kobayashi, A. N. Edelbrock,
825 T. Mashimo, C. A. Miller, T. L. McGuire, S. I. Stupp, J. A. Kessler,

- 826 Creating a stem cell niche in the inner ear using self-assembling peptide
827 amphiphiles., Plos One 12 (12) (2017) e0190150. doi:10.1371/journal.
828 pone.0190150.
- 829 [24] A. J. Matsuoka, Z. D. Morrissey, C. Zhang, K. Homma, A. Belmadani,
830 C. A. Miller, D. M. Chadly, S. Kobayashi, A. N. Edelbrock, M. Tanaka-
831 Matakatsu, D. S. Whitlon, L. Lyass, T. L. McGruire, S. I. Stupp, J. A.
832 Kessler, Directed Differentiation of Human Embryonic Stem Cells Toward
833 Placode-Derived Spiral Ganglion-Like Sensory Neurons, Stem Cells Trans-
834 lational Medicine 6 (2017) 923–936. doi:10.1002/sctm.16-0032.
- 835 [25] H. Al-Ali, S. R. Beckerman, J. L. Bixby, V. P. Lemmon, In vitro models
836 of axon regeneration, Experimental Neurology 287 (Pt 3) (2017) 423–434.
837 doi:10.1016/j.expneurol.2016.01.020.
- 838 [26] U. K. Laemmli, Cleavage of structural proteins during the assembly of
839 the head of bacteriophage T4., Nature 227 (5259) (1970) 680–685. doi:
840 10.1038/227680a0.
- 841 [27] A. L. Mandel, H. Ozdener, V. Utermohlen, Identification of pro- and mature
842 brain-derived neurotrophic factor in human saliva., Archives of oral biology
843 54 (7) (2009) 689–695. doi:10.1016/j.archoralbio.2009.04.005.
- 844 [28] C. A. Schneider, W. S. Rasband, K. W. Eliceiri, NIH Image to ImageJ:
845 25 years of image analysis, Nature Methods 9 (7) (2012) 671–675. arXiv:
846 arXiv:1011.1669v3, doi:10.1038/nmeth.2089.
- 847 [29] R. W. Burry, Controls for immunocytochemistry: an update., The journal
848 of histochemistry and cytochemistry : official journal of the Histochemistry
849 Society 59 (1) (2011) 6–12. doi:10.1369/jhc.2010.956920.
- 850 [30] M. B. Mazalan, M. A. B. Ramlan, J. H. Shin, T. Ohashi, Effect of geomet-
851 ric curvature on collective cell migration in tortuous microchannel devices,
852 Micromachines 11 (7) (2020) 1–17. doi:10.3390/MI11070659.

- 853 [31] F. Xu, T. Beyazoglu, E. Hefner, U. A. Gurkan, U. Demirci, Automated
854 and adaptable quantification of cellular alignment from microscopic images
855 for tissue engineering applications, *Tissue Engineering - Part C: Methods*
856 17 (6) (2011) 641–649. doi:[10.1089/ten.tec.2011.0038](https://doi.org/10.1089/ten.tec.2011.0038).
- 857 [32] E. Batschelet, *Circular Statistics in Biology (Mathmatics in Biology Series)*,
858 1st Edition, Academic Press, New York, NY, 1981.
- 859 [33] P. Berens, M. J. Velasco, CircStat for Matlab: Toolbox for circular statistics
860 with Matlab, Max–Planck–Institut f ur biologische Kybernetik, Technical
861 Report No. 184 31 (10) (2009) 1–21. doi:[doi:10.18637/jss.v031.i10](https://doi.org/10.18637/jss.v031.i10).
- 862 [34] M. Pool, J. Thiemann, A. Bar-Or, A. E. Fournier, NeuriteTracer: A novel
863 ImageJ plugin for automated quantification of neurite outgrowth, *Journal*
864 of Neuroscience Methods 168 (1) (2008) 134–139. doi:[10.1016/j.jneumeth.2007.08.029](https://doi.org/10.1016/j.jneumeth.2007.08.029).
- 866 [35] E. Meijering, M. Jacob, J.-C. F. Sarria, P. Steiner, H. Hirling, M. Unser,
867 Design and validation of a tool for neurite tracing and analysis in fluo-
868 rescence microscopy images., *Cytometry. Part A : the journal of the In-*
869 *ternational Society for Analytical Cytology* 58 (2) (2004) 167–176. doi:
870 [10.1002/cyto.a.20022](https://doi.org/10.1002/cyto.a.20022).
- 871 [36] M. Anniko, W. Arnold, T. Stigbrand, A. Strom, The Human Spiral Gan-
872 glion, *ORL* 57 (1995) 68–77.
- 873 [37] S. van der Walt, S. C. Colbert, G. Varoquaux, The NumPy Array: A
874 Structure for Efficient Numerical Computation, *Computing in Science En-*
875 *gineering* 13 (2) (2011) 22–30. doi:[10.1109/MCSE.2011.37](https://doi.org/10.1109/MCSE.2011.37).
- 876 [38] J. D. Hunter, Matplotlib: A 2D Graphics Environment, *Computing in*
877 *Science Engineering* 9 (3) (2007) 90–95. doi:[10.1109/MCSE.2007.55](https://doi.org/10.1109/MCSE.2007.55).
- 878 [39] P. Virtanen, R. Gommers, T. E. Oliphant, M. Haberland, T. Reddy,
879 D. Cournapeau, E. Burovski, P. Peterson, W. Weckesser, J. Bright, S. J.

- van der Walt, M. Brett, J. Wilson, K. J. Millman, N. Mayorov, A. R. J. Nelson, E. Jones, R. Kern, E. Larson, C. J. Carey, I. Polat, Y. Feng, E. W. Moore, J. VanderPlas, D. Laxalde, J. Perktold, R. Cimrman, I. Henriksen, E. A. Quintero, C. R. Harris, A. M. Archibald, A. H. Ribeiro, F. Pedregosa, P. van Mulbregt, SciPy 1.0: fundamental algorithms for scientific computing in Python., *Nature methods* 17 (3) (2020) 261–272.
[doi:10.1038/s41592-019-0686-2](https://doi.org/10.1038/s41592-019-0686-2).
- [40] P. Berens, CircStat : A MATLAB Toolbox for Circular Statistics , *Journal of Statistical Software* 31 (10). [doi:10.18637/jss.v031.i10](https://doi.org/10.18637/jss.v031.i10).
- [41] M. Tuncel, H. S. Sürücü, K. M. Erbil, A. Konan, Formation of the cochlear nerve in the modiolus of the guinea pig and human cochleae., *Archives of medical research* 36 (5) (2005) 436–40. [doi:10.1016/j.arcmed.2005.02.003](https://doi.org/10.1016/j.arcmed.2005.02.003).
- [42] B. Küçük, K. Abe, T. Ushiki, Y. Inuyama, S. Fukuda, Kazuo Ishikawa, Microstructures of the Bony Modiolus in the Human Cochlea : A Scanning Electron Microscopic Study, *Journal of Electron Microsc* 40 (40) (1991) 193–197.
- [43] O. Levenspiel, Chemical Reaction Engineering, 3rd Edition, John Wiley and Sons, Inc., New York, NY, 1999.
- [44] M. Stroh, W. R. Zipfel, R. M. Williams, S. C. Ma, W. W. Webb, W. M. Saltzman, Multiphoton microscopy guides neurotrophin modification with poly(ethylene glycol) to enhance interstitial diffusion, *Nature Materials* 3 (7) (2004) 489–494. [doi:10.1038/nmat1159](https://doi.org/10.1038/nmat1159).
- [45] S. Axler, Linear Algebra Done Right, 3rd Edition, Springer Publishing, New York, NY, 2015.
- [46] J. Crank, The mathematics of Diffusion, 2nd Edition, Oxford University Press, London, UK, 1979.

- 907 [47] K. M. Keefe, I. S. Sheikh, G. M. Smith, Targeting Neurotrophins to Specific
908 Populations of Neurons: NGF, BDNF, and NT-3 and Their Relevance
909 for Treatment of Spinal Cord Injury., International journal of molecular
910 sciences 18 (3). doi:10.3390/ijms18030548.
- 911 [48] B. I. Awad, M. A. Carmody, M. P. Steinmetz, Potential role of growth
912 factors in the management of spinal cord injury., World Neurosurgery 83 (1)
913 (2015) 120–131. doi:10.1016/j.wneu.2013.01.042.
- 914 [49] E. R. n. Hollis, M. H. Tuszyński, Neurotrophins: potential therapeutic tools
915 for the treatment of spinal cord injury., Neurotherapeutics : the journal of
916 the American Society for Experimental NeuroTherapeutics 8 (4) (2011)
917 694–703. doi:10.1007/s13311-011-0074-9.
- 918 [50] A. H. Nagahara, B. R. Wilson, I. Ivasyk, I. Kovacs, S. Rawalji, J. R.
919 Bringas, P. J. Piviroto, W. S. Sebastian, L. Samaranch, K. S. Bankiewicz,
920 M. H. Tuszyński, MR-guided delivery of AAV2-BDNF into the entorhi-
921 nal cortex of non-human primates., Gene therapy 25 (2) (2018) 104–114.
922 doi:10.1038/s41434-018-0010-2.
- 923 [51] S. D. Croll, C. Suri, D. L. Compton, M. V. Simmons, G. D. Yan-
924 copoulos, R. M. Lindsay, S. J. Wiegand, J. S. Rudge, H. E. Scharfman,
925 Brain-derived neurotrophic factor transgenic mice exhibit passive avoid-
926 ance deficits, increased seizure severity and in vitro hyperexcitability in
927 the hippocampus and entorhinal cortex., Neuroscience 93 (4) (1999) 1491–
928 1506. doi:10.1016/s0306-4522(99)00296-1.
- 929 [52] A. Dravid, S. Parittotokkaporn, Z. Aqrawe, S. J. O’Carroll, D. Svirskis,
930 Determining Neurotrophin Gradients in Vitro to Direct Axonal Outgrowth
931 following Spinal Cord Injury, ACS Chemical Neuroscience 11 (2) (2020)
932 121–132. doi:10.1021/acschemnuro.9b00565.
- 933 [53] T. Yamagata, J. M. Miller, M. Ulfendahl, N. P. Olivius, R. A. Altschuler,
934 I. Pyykkö, G. Bredberg, Delayed neurotrophic treatment preserves nerve

- 935 survival and electrophysiological responsiveness in neomycin-deafened
936 guinea pigs., Journal of neuroscience research 78 (1) (2004) 75–86. doi:
937 10.1002/jnr.20239.
- 938 [54] M. P. Zanin, M. Hellstr??m, R. K. Shepherd, A. R. Harvey, L. N. Gillespie,
939 Development of a cell-based treatment for long-term neurotrophin expres-
940 sion and spiral ganglion neuron survival, Neuroscience 277 (2014) 690–699.
941 doi:10.1016/j.neuroscience.2014.07.044.
- 942 [55] M. Seyyedi, L. Viana, J. J. Nadol, Within-subject comparison of word
943 recognition and spiral ganglion cell count in bilateral cochlear implant
944 recipients, Otol Neurotol 35 (8) (2014) 1446–1450. doi:10.1097/MAO.
945 000000000000443.Within-Subject.
- 946 [56] A. Henriques, C. Pitzer, A. Schneider, Neurotrophic growth factors for the
947 treatment of amyotrophic lateral sclerosis: where do we stand?, Frontiers
948 in neuroscience 4 (2010) 32. doi:10.3389/fnins.2010.00032.
- 949 [57] J. F. Poduslo, G. L. Curran, Permeability at the blood-brain and
950 blood-nerve barriers of the neurotrophic factors: NGF, CNTF, NT-3,
951 BDNF, Molecular Brain Research 36 (2) (1996) 280–286. doi:10.1016/
952 0169-328X(95)00250-V.
- 953 [58] T. Sakane, W. M. Pardridge, Carboxyl-directed pegylation of brain-derived
954 neurotrophic factor markedly reduces systemic clearance with minimal loss
955 of biologic activity (1997). doi:10.1023/A:1012117815460.
- 956 [59] R. G. Soderquist, E. D. Milligan, E. M. Sloane, J. A. Harrison, K. K.
957 Douvas, J. M. Potter, T. S. Hughes, R. A. Chavez, K. Johnson, L. R.
958 Watkins, M. J. Mahoney, PEGylation of brain-derived neurotrophic factor
959 for preserved biological activity and enhanced spinal cord distribution.,
960 Journal of biomedical materials research. Part A 91 (3) (2009) 719–729.
961 doi:10.1002/jbm.a.32254.

- 962 [60] M. Sasi, B. Vignoli, M. Canossa, R. Blum, Neurobiology of local and inter-
963 cellular BDNF signaling, *Pflugers Archiv : European journal of physiology*
964 469 (5-6) (2017) 593–610. doi:10.1007/s00424-017-1964-4.
- 965 [61] X. Li, Y. Su, S. Liu, L. Tan, X. Mo, S. Ramakrishna, Encapsulation
966 of proteins in poly(l-lactide-co-caprolactone) fibers by emulsion electro-
967 spinning, *Colloids and Surfaces B: Biointerfaces* 75 (2) (2010) 418–424.
968 doi:10.1016/j.colsurfb.2009.09.014.
- 969 [62] E. E. L. Swan, M. Peppi, Z. Chen, K. M. Green, J. E. Evans, M. J.
970 McKenna, M. J. Mescher, S. G. Kujawa, W. F. Sewell, Proteomics analysis
971 of perilymph and cerebrospinal fluid in mouse., *The Laryngoscope* 119 (5)
972 (2009) 953–958. doi:10.1002/lary.20209.
- 973 [63] T. Numakawa, S. Suzuki, E. Kumamaru, N. Adachi, M. Richards,
974 H. Kunugi, BDNF function and intracellular signaling in neurons, *Histology
975 and Histopathology* 25 (2) (2010) 237–258. doi:10.14670/HH-25.237.
- 976 [64] C. Gentile, Engineering of Spheroids for Stem Cell Technology, *Current
977 Stem Cell Research & Therapy* 11 (2016) 652–665. doi:10.2174/
978 1574888x10666151001114848.
- 979 [65] H. Berg, *Random Walks in Biology*, Princeton Universtiyy Press, Prinston,
980 NJ, 1983.
- 981 [66] H. Li, F. Edin, H. Hayashi, O. Gudjonsson, N. Danckwardt-Lillies, H. En-
982 gqvist, H. Rask-Andersen, W. Xia, Guided growth of auditory neurons:
983 Bioactive particles towards gapless neural electrode interface, *Biomaterials*
984 122 (2017) 1–9. doi:10.1016/j.biomaterials.2016.12.020.
- 985 [67] J. Schulze, H. Staeker, D. Wedekind, T. Lenarz, A. Warnecke, Expression
986 pattern of brain-derived neurotrophic factor and its associated receptors:
987 Implications for exogenous neurotrophin application., *Hearing Research* 413
988 (2020) 108098. doi:10.1016/j.heares.2020.108098.